



CHORUS

This is the accepted manuscript made available via CHORUS. The article has been published as:

Flow-radiation coupling in CO₂ hypersonic wakes using reduced-order non-Boltzmann models

Amal Sahai, Christopher O. Johnston, Bruno Lopez, and Marco Panesi

Phys. Rev. Fluids **4**, 093401 — Published 20 September 2019

DOI: [10.1103/PhysRevFluids.4.093401](https://doi.org/10.1103/PhysRevFluids.4.093401)

Flow-Radiation Coupling in CO₂ Hypersonic Wakes using Reduced-order Non-Boltzmann Models

Amal Sahai

University of Illinois at Urbana-Champaign, IL, USA.

Christopher O. Johnston

NASA Langley Research Center, VA, USA.

Bruno Lopez and Marco Panesi*

University of Illinois at Urbana-Champaign, IL, USA.

(Dated: September 8, 2019)

Abstract

The current work presents a computationally tractable simulation methodology combining different model-reduction techniques for resolving non-Boltzmann thermodynamics, chemical kinetics, and radiative transfer in complex three-dimensional flows. The empiricism associated with conventional multi-temperature non-equilibrium models is abandoned in favor of the multi-group maximum entropy method combined with kinetics-informed adaptive binning. This group-based approach allows for time-varying optimal reduced-order representation of the internal state population distribution while accounting for all collisional processes included in the state-to-state model. Similarly, radiative transfer calculations are performed efficiently by discretization in the spectral, angular, and spatial spaces using the smeared band, discrete ordinate, and finite volume methods respectively. This reduction in computational overhead allows truly non-Boltzmann simulations with two-way coupling between the flow and radiation fields to be realized without simplifying approximations based on the tangent-slab method or local escape-factors. The new simulation procedure is used in conjunction with the US3D flow solver to investigate the impact of vibrational non-equilibrium on CO₂ wake flows and resultant infrared radiation around the Mars 2020 vehicle. This involves comparing predictions for flowfield properties and radiative transfer obtained using the conventional two-temperature model, multi-group non-Boltzmann model, and for decoupled/coupled flow-radiation calculations. Conventional two-temperature models overestimate the rate of thermal equilibration in the near-wake region resulting in the population of mid-lying and upper CO₂ vibrational levels being underpredicted by multiple orders of magnitude. Additionally, the two-temperature approach (in comparison to bin-based StS) overpredicts the rate of CO₂ dissociation thereby leading to erroneous estimates for flow properties in the post-shock region (primary source of afterbody radiative emission). This results in inflated values for surface radiative heat flux with two-temperature modeling, although overall differences in radiative behavior are

tempered by the fast characteristic relaxation times for ground vibrational levels.

I. INTRODUCTION

A key step in the development of reliable and cost-effective thermal protection systems for shielding spacecraft from the rigors of hypersonic planetary entry is accurate characterization of thermal and aerodynamic force loads [1]. A combination of high freestream enthalpy and rarefied atmospheric conditions can result in the flow surrounding the spacecraft being dominated by non-equilibrium phenomena. The rapid dissipation of flow kinetic energy downstream of the shock drives energetic collisions and radiative transitions [2]. Collisional-radiative (CR) processes drive both local and non-local (absorption of radiative intensity) thermochemical changes in the flowfield resulting in excitation of internal energy modes, dissociation, and ionization of gas particles [2]. The impact of radiation on flowfield properties and flight characteristics grows in significance with entry speeds. Recent work on Martian atmospheric entry [3–6] indicates that CO₂ infrared radiation (IR) dominates the total heat flux received by the backshell of spacecraft. Thus, as heat shields are designed with more aggressive safety margins, accurately resolving complex thermochemical and radiative phenomena is of paramount importance.

Thermal and chemical non-equilibrium has traditionally been modeled using semi-empirical models that suffer from two key shortcomings. Firstly, they introduce arbitrary empiricism by relying on parameters calibrated to reproduce experimental data obtained for only a limited range of test conditions. Secondly, the underlying physics of non-equilibrium is simplified through assumptions such as a rigid separation of the internal energy modes (translational, rotational, vibrational, and

* Author to whom correspondence should be addressed: mpanesi@illinois.edu

electronic) and defining one or multiple temperatures to describe the population of each internal energy level [7]. Consequently, most state-of-the-art approaches applied to computational fluid dynamics (CFD) simulations are fundamentally incapable of capturing complex non-equilibrium internal distributions characterized by different features for the low lying, mid-to-high lying and pre-dissociated states [8–10].

The current study aims to efficiently incorporate detailed state-to-state (StS) models, thereby enabling large-scale predictive simulations. The increasing availability of first-principles based rate data for microscopic interactions between individual quantum states [11–14] opens the door to accurate characterization of non-equilibrium state population distributions. However, full StS models are prohibitively expensive even for the simple physical problems. Coarse grain models which group individual levels together into a reduced number of macroscopic bins (the term bins and groups are used interchangeably) have been used previously to overcome this impediment [15–17]. The work by Liu *et al.* [18] – referred to as the multi-group maximum entropy method (MGME) – establishes a mathematically rigorous formulation for the time evolution of macroscopic bin properties (population, energy, and higher-order moments) while retaining all microscopic processes from the StS model. Unlike StS models, population of individual states no longer serve as system unknowns. Instead, they are reconstructed using bin-specific distribution functions that maximize entropy and are constrained by bin properties. The reduced system of governing equations for bin properties is derived by summing up moments of the StS master equations. The multi-group maximum entropy method has been further improved through the introduction of grouping strategies informed by kinetics (referred to as adaptive binning) [19]. State-to-state processes with different characteristic time-scales are modeled with varying degrees of fidelity which results in better predictions for transient behavior borne out of selective equilibration of internal energy levels [19, 20]. The current study uses the multi-group maximum entropy

method in conjunction with adaptive binning to strike a balance between accuracy and computational tractability while describing non-equilibrium dynamics.

Radiative emissions are strongly dependent on the exact internal state population distribution [21] and therefore, non-Boltzmann deviations in expanding wakes can dramatically alter radiative heat transfer. Additionally, radiative transitions themselves can alter populations for individual states of radiating gaseous species through local emission and absorption of the globally determined radiative intensity. This two-way coupling makes it imperative that thermochemistry and radiation be dealt with in a unified manner. The first step in achieving this is by allowing non-Boltzmann bin-based distributions (in addition to other bulk properties) from flowfield calculations to be used for computing spectral properties from state-specific radiation databases. Analogous to StS modeling, the use of line-by-line approach [22] with $\mathcal{O}(10^6)$ frequency evaluations for a single line-of-sight is computationally impractical for multi-dimensional radiation fields. A range of model reduction techniques in frequency space have been employed previously [3, 4, 23–25] for solving radiative transfer for complex high-enthalpy flows. The current work extends the smeared band method [26] to compute spectral variation in absorption and emission behavior directly from non-Boltzmann bin properties. This consistency with the MGME method also avoids additional costs associated with unpacking bins into state-specific population distributions and then modeling state-to-state radiative transitions (traditionally done when introducing non-Boltzmann effects [27, 28]). The geometric aspect of radiation problems involving spatial and angular resolution of the radiative transfer equations (RTEs) is dealt with efficiently through finite-volume discretization [29, 30] and the discrete ordinate method [31, 32]. The aforementioned elements of the radiation solution procedure together allow a detailed treatment of reaction rates driven by local and non-local radiative transitions without resorting to conventional approximations based on escape factors [33] or tangent-slab method

for radiative intensity [21, 34].

Previous work on CO₂ wake flows and associated IR radiation [3–6] have been limited to the use of conventional multi-temperature models. Researchers have also modeled CO₂ vibrational non-equilibrium by defining independent temperatures for different modes (symmetric stretching, bending, asymmetric stretching) [25, 35]. These efforts are impeded by a common constraint – internal levels being forced into Boltzmann distributions – and the semi-empiricism that stems from it. Additionally, existing research on the subject completely disregards the two-way coupling between thermochemistry and radiative transitions, with the radiative field computed simply as a post-processing step. The current work represents the first attempt at holistically investigating the impact of self-consistent non-Boltzmann modeling on CO₂ thermochemistry and the resultant radiative behavior for hypersonic wake flows. Additionally, it characterizes the possible impact of non-local radiative emissions on CO₂ vibrational relaxation and bulk flow properties. This paper is organized as follows: a) Section II provides an overview of the vibrational-specific CO₂ thermochemistry model and the multi-bin model-reduction paradigm. b) Section III begins with a description of reduce-order spectral model for CO₂ radiation using the smeared band method [4, 36]. This is followed by an outline of angular/spatial discretization techniques for solving radiative transfer equations (RTEs). This section concludes with the self-consistent model for the two-way coupling between flow phenomena and radiation. c) The hydrodynamic governing equations are discussed in Section IV. d) Numerical studies are conducted on the Mars 2020 vehicle by applying the proposed non-equilibrium methodology to the US3D flow solver [37–39]. Section V presents a detailed analysis of flow structures, thermochemistry, and radiative transfer in the afterbody region of the spacecraft. e) Lastly, the conclusions are summarized in Section VI.

II. THERMOCHEMISTRY MODEL

A. State-to-state Thermodynamics and Kinetics of CO₂

The current non-equilibrium framework incorporates the vibrational state-to-state thermochemistry model developed by Kustova *et al.* [14, 40, 41]. Electronic excitation is neglected and only the ground electronic state CO₂(X¹Σ_g⁺) is considered. Carbon dioxide is a linear molecule and possesses four vibrational modes – one symmetric stretching mode, two degenerate bending modes, and one asymmetric stretching mode. The energy of individual CO₂ vibrational levels is described using the anharmonic oscillator expression [42]:

$$E_{v_1, v_2, v_3} / (\text{hc}) = \sum_{k=1}^3 \omega_k \left(v_k + \frac{d_k}{2} \right) + \sum_{k=1}^3 \sum_{j \geq k}^3 \chi_{kj} \left(v_k + \frac{d_k}{2} \right) \left(v_j + \frac{d_j}{2} \right) + \sum_{k=1}^3 \sum_{j \geq k}^3 \sum_{i \geq j \geq k}^3 y_{kji} \left(v_k + \frac{d_k}{2} \right) \left(v_j + \frac{d_j}{2} \right) \left(v_i + \frac{d_i}{2} \right) + \dots \quad (1)$$

where h is the Planck constant, c is the speed of light, and the indices i , j and k define parameters associated with the symmetric, bending, and asymmetric vibrational modes respectively. Spectroscopic constants such as ω_k , χ_{kj} , and y_{kji} that appear in Eq. 1 are obtained from experimental data [43]. The vibrational quantum number and corresponding degeneracy for mode i are denoted by v_i and d_i respectively. A simplified form of the anharmonic oscillator expression is employed which retains only the first three summation terms in Eq. (1) and neglects higher order contributions. The existence of multiple vibrational modes allows states with otherwise distinctly different vibrational quantum numbers to have comparable energies which has a strong impact on the dynamics of the population distribution function. Furthermore, the maximum vibrational energy is limited to the dissociation energy of CO₂(X¹Σ_g⁺), resulting in 9,056 unique levels.

The complex internal structure of the CO_2 molecule results in a rich set of disparate reaction mechanisms that shape vibrational relaxation. Quantum selection rules precludes inelastic interactions between the translational and symmetric/asymmetric modes. Thus, vibrational-translational equilibration occurs through transitions involving only the bending mode, which leave the other two modes unchanged:



where M denotes the collision partner whose internal state remains unaltered during the reaction. The next category of collisional processes considered are inter-modal VV_{m-k} exchanges resulting in energy transfer between two or more vibrational modes:



In order to limit computational challenges in this introductory study into non-Boltzmann effects on three-dimensional flowfields and IR radiation, the authors have considered StS modeling for a single species – CO_2 . Thus, only collisional processes that are defined between vibrational states of CO_2 but do not require a StS description for other species are incorporated into the current kinetic scheme. With a robust simulation framework now in place, additional transitions including state-specific energy exchange with species such as CO and O_2 will be considered in future studies [44]. Finally, state-specific dissociation/recombination reactions are also added to the kinetic scheme:



Collision partners considered in the current study include C, CO, O₂, and CO₂ (total population of carbon-dioxide). A common bottleneck while developing CO₂ StS models is the paucity of state-specific rate data available in open literature. Additionally, experimental data is only available for transitions between the lowest energy states. It is imperative that low energy experimental data be combined with existing theoretical models to yield a self-consistent StS chemistry database. Consequently, the hybrid approach propounded by Kustova and Nagnibeda [40, 41, 45] is used for computing rate coefficients for vibrational states of CO₂: a) rate coefficient data for transitions between the lowest vibrational states are obtained directly from experimental measurements, b) rate coefficients for higher states are calculated using SSH theory modified for polyatomic molecules. Lastly, the global dissociation rate constant (legacy values outlined in [7, 46]) is unpacked into state-specific values using a generalized form of the Treanor – Marrone model [47].

B. Adaptive Bin-based Reduced-order Modeling

The application of StS models to practical multi-dimensional computational fluid dynamics (CFD) problems is unfeasible due to high computational costs. The present work overcomes this limitation through the use of the multi-group maximum entropy method [18] in conjunction with adaptive binning [19]. The process of model reduction can be broken down into two steps:

- **Local Representation and Reconstruction:** Individual internal energy levels are lumped into larger macroscopic energy bins. The population of grouped levels is reconstructed using bin-wise distribution functions that are defined using “macroscopic” quantities (bin population and energy).
- **Macroscopic Moment Equations and Rate Coefficients:** Governing

equations for “macroscopic” quantities are derived by taking successive moments of StS master equations and summing contributions for all internal states belonging to a common bin.

The use of bin-wise distribution functions allows complex state-to-state dynamics to be resolved with sufficient accuracy without the onerous cost of solving full set of master equations for individual levels. The following form for the distribution function is assumed:

$$\log \left(\frac{g_{\text{CO}_2}^v}{n_{\text{CO}_2}^v} \right) = \alpha_{\text{CO}_2}^b + \beta_{\text{CO}_2}^b \epsilon_{\text{CO}_2}^v, \quad \forall v \in \mathcal{I}_b \quad (7)$$

where $g_{\text{CO}_2}^v$ and $\epsilon_{\text{CO}_2}^v$ denote degeneracy and energy of state v . The set of vibrational states included in the b^{th} bin is denoted by \mathcal{I}_b . Bin-specific coefficients $\alpha_{\text{CO}_2}^b$ and $\beta_{\text{CO}_2}^b$ for the linear distribution function are formulated in terms of two “macroscopic” constraints – bin population $N_{\text{CO}_2}^b$ and energy $E_{\text{CO}_2}^b$ per unit volume – using the maximum entropy principle and the variational method outlined in [48]:

$$N_{\text{CO}_2}^b = \sum_{v \in \mathcal{I}_b} n_{\text{CO}_2}^v, \quad E_{\text{CO}_2}^b = \sum_{v \in \mathcal{I}_b} n_{\text{CO}_2}^v \epsilon_{\text{CO}_2}^v \quad (8)$$

where $n_{\text{CO}_2}^v$ and $\epsilon_{\text{CO}_2}^v$ are the population and energy densities respectively of the v^{th} state. The macroscopic bin properties defined in Eq. (8) are treated as unknowns for the reduced-order model (in lieu of the population of individual levels in the full StS model). The governing equations for the b^{th} bin (which includes excitation/de-excitation and dissociation/recombination processes) are derived by taking successive energy moments of the StS master equations and summing up individual equations corresponding to all states $v \in \mathcal{I}_b$:

$$\begin{aligned} \sum_{v \in \mathcal{I}_b} \frac{d n_{\text{CO}_2}^v}{dt} (\epsilon_{\text{CO}_2}^v)^m &= \sum_{i \in \text{exc}} \sum_M \sum_{v \in \mathcal{I}_b} \sum_{v' \in \mathcal{I}_c} \left[-\kappa_{v,v'}^{i,M} n_{\text{CO}_2}^v n_M (\epsilon_{\text{CO}_2}^v)^m + \kappa_{v',v}^{i,M} n_{\text{CO}_2}^{v'} n_M (\epsilon_{\text{CO}_2}^v)^m \right] \\ &+ \sum_M \sum_{v \in \mathcal{I}_b} \left[-\kappa_v^{d,M} n_{\text{CO}_2}^v n_M (\epsilon_{\text{CO}_2}^v)^m + \kappa_v^{r,M} n_{\text{CO}} n_{\text{O}} n_M (\epsilon_{\text{CO}_2}^v)^m \right] \quad (9) \end{aligned}$$

where $\kappa_{v,v'}^{i,M}$ and $\kappa_{v',v}^{i,M}$ are the forward and backward rate coefficients for the i^{th} type of excitation process and collision partner M between vibrational states v to v' . The state-specific dissociation and recombination rate-coefficients for collision partner M are denoted by $\kappa_v^{d,M}$ and $\kappa_v^{r,M}$. The total population densities of CO, O, and collision partner M are given by n_{CO} , n_{O} , and n_M respectively. The macroscopic equations for bin population and vibrational energy are obtained by setting order of the moment to $m = 0$ and $m = 1$ respectively:

$$\dot{\Omega}_{\text{col,CO}_2}^b \times N_A : \quad \frac{d}{dt} N_{\text{CO}_2}^b = \sum_{i \in \text{exc}} \sum_M \sum_c \left(- {}^0 K_{b,c}^{i,M} N_{\text{CO}_2}^b n_M + {}^0 \bar{K}_{c,b}^{i,M} N_{\text{CO}_2}^c n_M \right) + \sum_M \left(- {}^0 C_b^M N_{\text{CO}_2}^b n_M + {}^0 \bar{C}_b^M n_{\text{CO}} n_{\text{O}} n_M \right) \quad (10)$$

$$\dot{\Omega}_{\text{col,CO}_2}^b \times N_A : \quad \frac{d}{dt} E_{\text{CO}_2}^b = \sum_{i \in \text{exc}} \sum_M \sum_c \left(- {}^1 K_{b,c}^{i,M} E_{\text{CO}_2}^b n_M + {}^1 \bar{K}_{c,b}^{i,M} E_{\text{CO}_2}^c n_M \right) + \sum_M \left(- {}^1 C_b^M E_{\text{CO}_2}^b n_M + {}^1 \bar{C}_b^M n_{\text{CO}} n_{\text{O}} n_M \right) \quad (11)$$

where ${}^m K_{b,c}^{i,M}$ and ${}^m \bar{K}_{c,b}^{i,M}$ are the bin-averaged forward and backward rate coefficients for i^{th} excitation process (collision partner M) between bin b to bin c and N_A is Avogadro's number. The bin-averaged dissociation and recombination coefficients for the b^{th} bin are ${}^m C_b^M$ and ${}^m \bar{C}_b^M$ respectively. The bin-averaged rate coefficients are a function of the translational temperature of the mixture and bin internal temperature T_b . The bin internal temperature T_b is compute by performing a non-linear inversion on the average internal energy of the bin: $(E_{\text{CO}_2}^b / N_{\text{CO}_2}^b)$. Additional details on the multi-group maximum entropy method and computing bin-averaged rate coefficients can be found in [18].

The next paradigm in realizing more accurate bin-based reduced-order methods focuses on evolving a physic-based binning strategy that is guided by StS dynamics of the chemical system. Previous studies using linear bins for reduced-order modeling [18, 49] have relied on energy being the sole metric for grouping internal states

into bins. This “energy binning” approach involves partitioning the internal energy space into continuous non-overlapping intervals, each representing a macroscopic bin. Internal states are then assigned to an appropriate bin (interval) on the basis of their energies. The multi-group maximum entropy approach through the use of linear bin-wise distribution functions implicitly assumes that internal levels within a common bin are in a state of thermal equilibrium. Thus, energy-based binning, with the erroneous expectation that states with similar energies quickly equilibrate with respect to each other, can result in inaccurate solutions. This ad-hoc assumption can be eliminated through a more generalized approach that is based on correctly identifying clusters of internal levels that are connected by more probable transitions and therefore, thermalize faster amongst themselves. In the context of CO₂ StS kinetics, Kustova and Nagnibeda [40] have reported that the characteristic times of various vibrational relaxation processes (VT_2 , VV_{1-2} , VV_{2-3} , VV_{1-2-3}) can differ by multiple orders of magnitude. This localized equilibration behavior has also been observed in other chemical systems [19] with certain internal states, owing to energy and quantum chemistry considerations, being linked by preferential transition pathways that allow faster interactions. The current work utilizes the modified island algorithm [10, 19] to identify clusters of states interconnected directly or indirectly by “fast” processes.

The rate-coefficients for VV_{m-k} and VT_2 processes have been evaluated for two temperatures that are relevant for Martian wake flows – $T = 1,500$ K and $T = 5,000$ K – in Fig. 1. The 9,056 unique levels considered for the study are sorted by increasing energy and then described using a single global index v . The mode-specific quantum numbers are then defined as $\{v_1(v), v_2(v), v_3(v)\}$. The horizontal axis in Fig. 1 corresponds to the initial vibrational level v for a given StS excitation transition. It is evident that barring limited outliers, a clear separation exists between the bulk of VV_{m-k} and VT_2 processes. Rate-coefficient values for both 1,500 K and

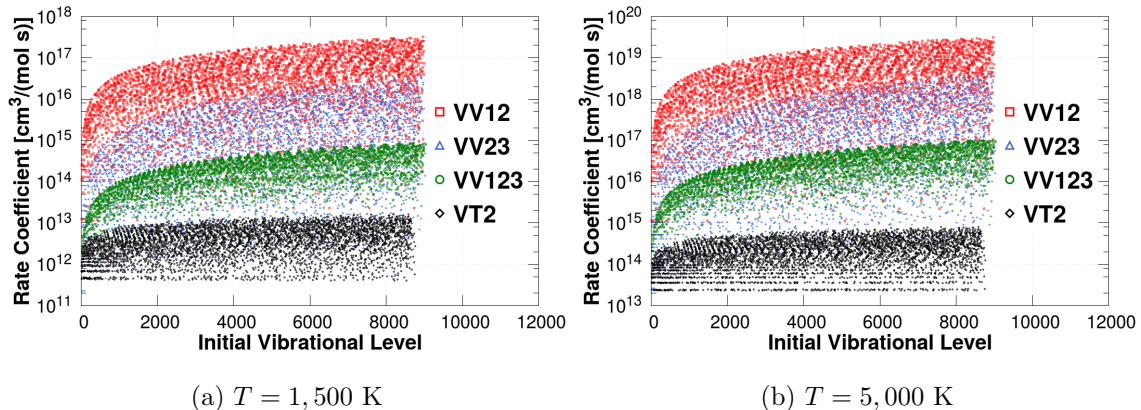


FIG. 1: Comparison of rate coefficients for inter-mode VV_{m-k} and vibrational-translational VT_2 excitation processes with $M = \text{CO}_2$.

5,000 K suggest that the most probable excitation pathways in descending order are VV_{1-2} , VV_{2-3} , VV_{1-2-3} , and VT_2 . This results in vibrational levels linked through VV_{m-k} transitions (rather than VT_2) thermalizing faster and reaching a state of localized equilibrium (as indicated by previous StS simulations for CO_2 [10]). Thus, VV_{1-2} , VV_{2-3} , and VV_{1-2-3} processes are classified as “fast” while binning the current StS system. Individual vibrational levels are initially divided into bins using the conventional energy-based strategy. The recursive island algorithm is then applied which moves all internal states connected by fast reactions into a common bin. It should be noted that the generalized approach outlined in [19] for effecting adaptive binning can be used in future studies for an expanded CO_2 StS kinetic scheme, where no clear apriori assertions about the relative difference between reaction characteristic time-scales can be made. This would involve identifying “fast” processes based on a numerically computed threshold value for rate-coefficients rather than the type of process being considered.

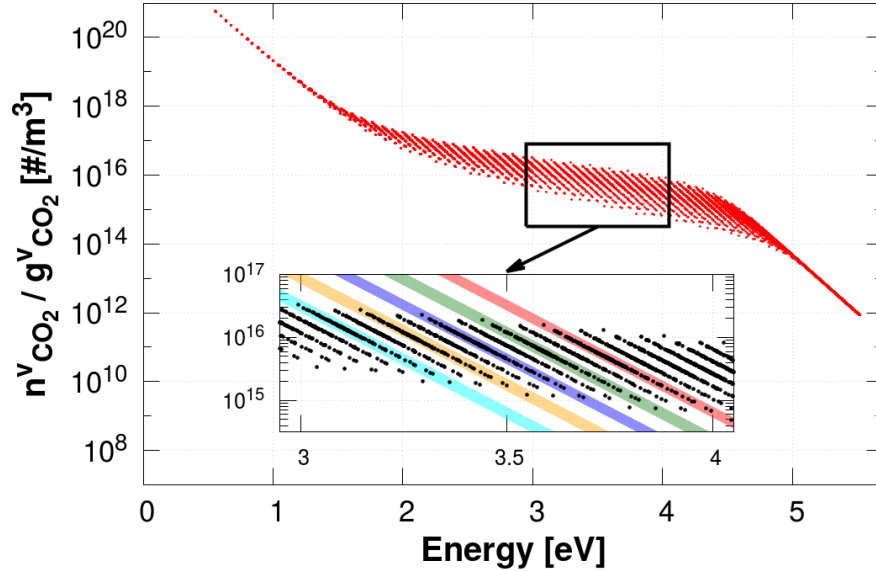


FIG. 2: Non-equilibrium CO_2 vibrational population at $t = 10^{-4}$ s computed using the full StS model in an ideal chemical reactor [10]. The inset figure magnifies the distinct comb-like structure of the non-equilibrium region.

A detailed assessment of the efficacy of the current reduced-order approach for CO_2 has been performed previously through unsteady simulations in an ideal chemical reactor [10]. Strong thermochemical non-equilibrium is induced by instantly changing the translational temperature T of the chemical reactor. The ensuing energy transfer and chemical change is then computed using both the full StS model and different reduced-order models (number of bins / binning strategies). A preliminary insight into non-Boltzmann behavior during rapid expansion in the wake region was gained by subjecting the idealized reactor to a sudden temperature drop from 5,000 K to 1,500 K. The vibrational state population distribution under such conditions is split into three different regions: a) the low energy states which rapidly reach their final equilibrium values, b) middle energy states that split into a com-

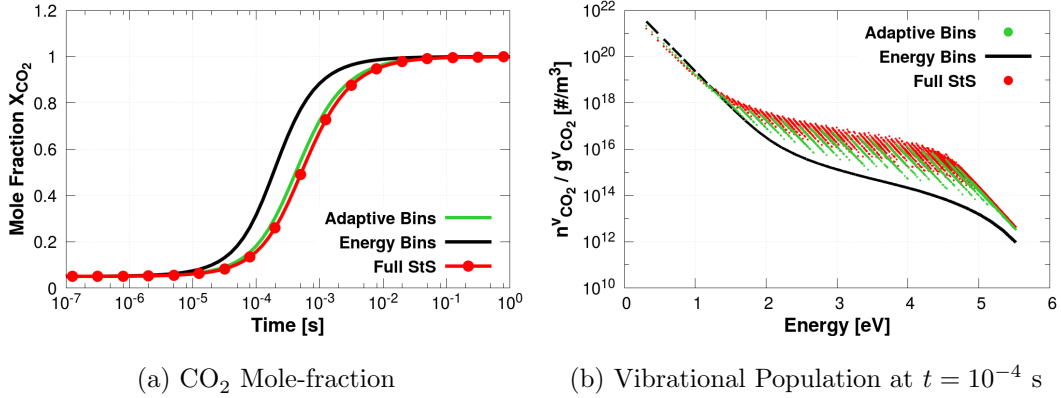


FIG. 3: Chemical reactor predictions for full StS, and reduced-order models based on 30 adaptive and energy bins [10].

plex non-Boltzmann cloud, c) and overpopulated high energy states. The comb-like non-equilibrium structure in the middle consists of multiple linear strands of states in local equilibrium. A detailed investigation of the quantum numbers of states that lie on the same linear thread in the non-equilibrium comb structure, *i.e.* within the same colored bounding box in Fig. 2, indicates that they are connected through either VV_{1-2} , VV_{2-3} , or VV_{1-2-3} processes. It is also observed that states in two adjacent strands are connected through the slower VT_2 processes. The thread-wise distribution strongly suggests that inter-modal VV_{m-k} transitions induce localized equilibration between connected vibrational states much more rapidly as compared to VT_2 exchanges.

Figure 3 presents the time-varying CO_2 mole-fraction and the vibrational population distribution at $t = 10^{-4}$ s computed using the full StS model (9056 levels), and reduced-order systems based on 30 adaptive and energy bins. A system of 10-30 adaptive bins (as opposed to the original energy-based binning), by accommodating for localized thermalization, is sufficient for accurately modeling both the state pop-

ulation distribution and macroscopic quantities of interest. It can be concluded that if the assumption of faster local equilibration through inter-modal VV_{m-k} transitions was for the most part invalid, the resultant adaptive binning MGME models (as is the case with energy binning) would not be able to replicate the dynamics of the original StS model. The bulk behavior of the 30 adaptive bin reduced-order model is analyzed by computing global dissociation coefficient for the quasi-steady state (QSS) distribution and characteristic vibrational relaxation times. These values are obtained using the ideal chemical reactor while considering VV_{m-k} , VT_2 , and dissociation/recombination (only for QSS dissociation rate) processes for a given collision partner. Good agreement with experimental data for CO_2 collated in [7, 50, 51] is obtained (Fig. 4), further bolstering confidence in the CO_2 StS model and the reduced-order system derived from it.

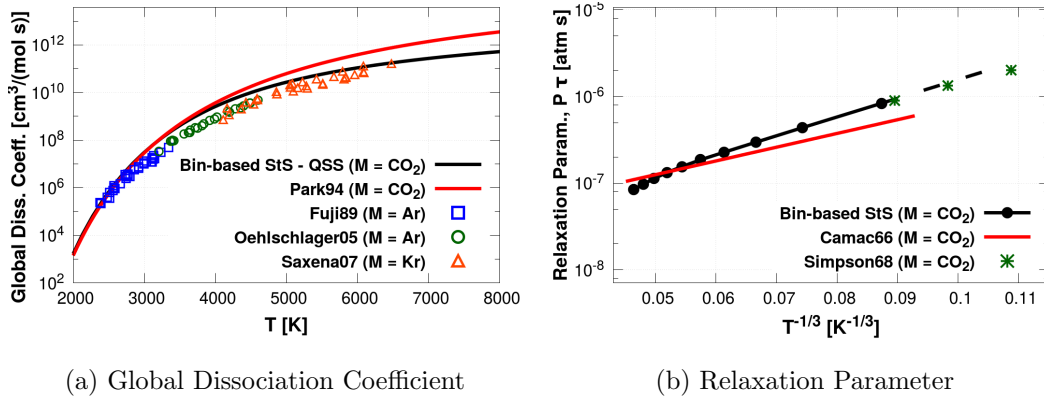


FIG. 4: Comparison of reduced-order model characteristics with experimental data (dashed lines represent extrapolated values).

III. RADIATION MODELING

A. Radiation database for CO₂

The approximately 400 million radiative transitions for CO₂ included in the CDSD-4000 database [52] are reduced into a convenient spectral model based on the smeared band method [4, 26]. This reduced-order spectral model is developed as a function of frequency, temperature, lower rovibrational level, and upper rovibrational level. To compile the smeared band spectrum, the absorption cross-sections within spectral grid intervals of 1 cm⁻¹ are summed as follows [26]:

$$\sigma_{\nu}^{i-j}(T_V) = \sum_{\nu_{CL} \in \nu + \Delta\nu} \left(\frac{I_{\text{CDSD}}^{i-j}}{\Delta\nu} \frac{1}{1 - \exp[-h_P \nu / (k_B T_{ref})]} \frac{Q_{\text{RV}}(T_{ref})}{Q_{\text{RV}}(T_V)} \frac{\exp[-\epsilon_{\text{CO}_2}^{i,\text{RV}} / (k_B T_V)]}{\exp[-\epsilon_{\text{CO}_2}^{i,\text{RV}} / (k_B T_{ref})]} \right) \quad (12)$$

where i and j represent the lower and upper rovibrational levels of the transition respectively, $\epsilon_{\text{CO}_2}^{i,\text{RV}}$ is the rovibrational energy of the i^{th} level, and Q_{RV} is the CO₂ total rovibrational partition function. The normalized absorption cross-sections in Eq. 12 can simply be scaled by total CO₂ number density N_{CO_2} to obtain the absorption/emission terms for rovibrational levels in a Boltzmann distribution at temperature T_V . The breakdown of the Boltzmann equilibrium assumption requires the following non-equilibrium correction factor for rovibrational level number densities [33]:

$$\phi^{i-j} = \frac{n_{\text{CO}_2}^j}{n_{\text{CO}_2}^{j,\text{Bol}}} \frac{n_{\text{CO}_2}^{i,\text{Bol}}}{n_{\text{CO}_2}^i} = \frac{n_{\text{CO}_2}^j}{n_{\text{CO}_2}^i} \frac{g_{\text{CO}_2}^{i,\text{RV}}}{g_{\text{CO}_2}^{j,\text{RV}}} \exp \left[\frac{-(\epsilon_{\text{CO}_2}^{i,\text{RV}} - \epsilon_{\text{CO}_2}^{j,\text{RV}})}{k_B T_V} \right] \quad (13)$$

where $n_{\text{CO}_2}^j$ and $n_{\text{CO}_2}^{j,\text{Bol}}$ are the predicted (could be non-Boltzmann) and corresponding Boltzmann (at T_V) rovibrational number densities respectively and $g_{\text{CO}_2}^{i,\text{RV}}$ is the degeneracy of the i^{th} rovibrational level. Using ϕ , the absorption ($\kappa_{\nu}^{i,j}$) and emission

$(j^{i,j})$ spectrum is defined in terms of $\sigma_\nu^{i,j}$ as follows [33, 53]:

$$\kappa_\nu^{i-j} = \frac{n_{\text{CO}_2}^i}{n_{\text{CO}_2}^{i,\text{Bol}}} N_{\text{CO}_2} \sigma_\nu^{i-j} \{1 - \phi^{i-j} \exp[-h_P \nu / (k_B T_V)]\} \quad (14)$$

$$J_\nu^{j-i} = \kappa_\nu^{i-j} \frac{2h_P \nu^3}{c^2} \frac{\phi^{i-j}}{\{\exp[h_P \nu / (k_B T_V)] - \phi^{i-j}\}} \quad (15)$$

These relationships indicate that only σ_ν^{i-j} needs to be pre-computed as a function of frequency and T_V for each combination of i and j . This represents an excessive amount of data which is not even immediately congruous with the current vibrational-specific chemistry model. The first step in mitigating these shortcomings is splitting the total rovibrational energy into rotational $\epsilon_{\text{CO}_2}^{i,\text{R}}$ and vibrational $\epsilon_{\text{CO}_2}^{i,\text{V}}$ contributions. The quantum state of internal state i is defined as $\{v(i), J(i)\}$, where $v(i)$ and $J(i)$ represent the vibrational and rotational configurations respectively. The vibrational and rotational components are considered to be uncorrelated. The energy of the rotational mode is computed using the rigid-rotor model [54]. These approximations also posit that the number of possible rotational configurations (and their corresponding energies/degeneracies) is the same for each vibrational state. Furthermore, since this study focuses on low-speed Martian entry which previous studies indicate experiences little thermal non-equilibrium [4], the rotational mode is assumed to be in equilibrium at T_V as well. The total CO_2 partition function Q_{RV} can be expressed as the product of the rotational Q_{R} (rigid-rotor) and vibrational Q_{V} (from StS level list) parts.

The state-specific description for σ_ν^{i-j} is reduced further by introducing assumptions enshrined in MGME framework. Thus, vibrational levels are assumed to be in a state of thermal equilibrium (at T_V) within their respective bins, whereas rotational modes continue remaining in equilibrium at T_V . The reconstructed number density is:

$$n_{\text{CO}_2}^i = N_{\text{CO}_2}^l \frac{g_{\text{CO}_2}^{i,\text{RV}} \exp\{-\epsilon_{\text{CO}_2}^{i,\text{R}} / (k_B T_V)\} \exp\{-\epsilon_{\text{CO}_2}^{i,\text{V}} / (k_B T_V)\}}{\hat{Q}_{\text{RV}}^l} \quad (16)$$

where vibrational level $v(i)$, corresponding to rovibrational state i , belongs to the l^{th} bin and $N_{\text{CO}_2}^l$ is the requisite bin density. The rotational contribution is constant for all bins. On the other hand, vibrational component \hat{Q}_V^l is obtained by summing over all individual vibrational levels included in the l^{th} bin. This bin-wise thermalization assumption allows an aggregate absorption cross-section to be defined, combining all radiative transitions from vibrational levels in bins l to u :

$$\hat{\sigma}_\nu^{l-u} = \sum_{\substack{\forall j \\ v(j) \in \mathcal{I}_u}} \sum_{\substack{\forall i \\ v(i) \in \mathcal{I}_l}} \sigma_\nu^{i-j} \frac{Q_{\text{RV}}}{\hat{Q}_{\text{RV}}^l} = \sum_{\substack{\forall j \\ v(j) \in \mathcal{I}_u}} \sum_{\substack{\forall i \\ v(i) \in \mathcal{I}_l}} \sigma_\nu^{i-j} \frac{Q_V}{\hat{Q}_V^l} \quad (17)$$

where \mathcal{I}_u and \mathcal{I}_l represent the set of vibrational levels included in bins u and l respectively. The bin-invariant rotational partition function cancels out. Thus, rotational component, with the assumption that it is uncorrelated with vibrational configuration, never needs to be separately evaluated while computing the aggregate cross-section and the resultant radiative properties. The bin-pair absorption and emission coefficients are obtained in a straightforward manner after scaling with the appropriate bin density (instead of total CO_2 density):

$$\hat{\kappa}_\nu^{l-u} = N_{\text{CO}_2}^l \hat{\sigma}_\nu^{l-u} \{1 - \phi^{l-u} \exp[-h_P \nu / (k_B T_V)]\} \quad (18)$$

$$\hat{j}_\nu^{u-l} = \hat{\kappa}_\nu^{l-u} \frac{2h_P \nu^3}{c^2} \frac{\phi^{l-u}}{\{\exp[h_P \nu / (k_B T_V)] - \phi^{l-u}\}} \quad (19)$$

The non-equilibrium correction factor ϕ^{l-u} is now computed using the predicted and corresponding Boltzmann bin number densities. Using these equations, emission coefficients for the $4.5 \mu\text{m}$ band originating from a Boltzmann distribution at $4,100 \text{ K}$ for different bin-pairs and normalized for number density are presented in Fig. 5.

Although the smeared band assumption can become inaccurate in optically-thick regions (error in total surface radiative flux upto 20%), these discrepancies are significantly smaller in the afterbody region which is characterized by intermediate optical thickness. Moreover, any bias introduced through the smeared band method relative

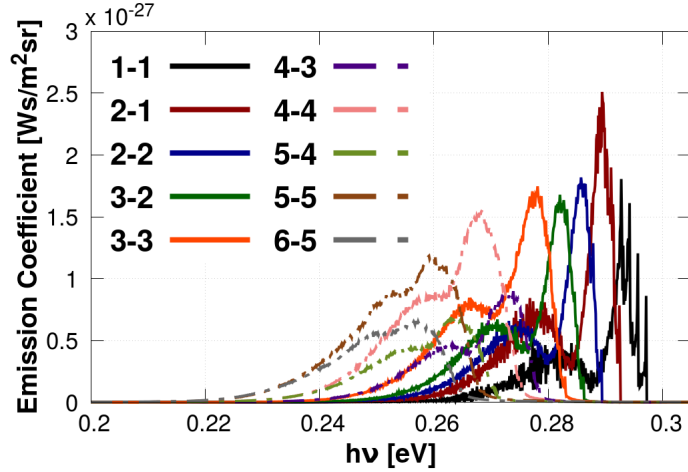


FIG. 5: Normalized emission coefficients for the $4.5 \mu\text{m}$ band originating from a Boltzmann distribution at $T_V = 4, 100$ K.

to line-by-line modeling is the same for both the reduced-order StS and conventional flow simulations. Therefore, the spectral modeling approach presented here represents a computationally efficient means of enabling consistent comparisons between the two flowfield models and isolating the impact of non-Boltzmann population distributions. It should be noted that implementing any alternative spectral model such as line-by-line approach, opacity-binning [55] or statistical narrow-band [23] would only require modifications to Eq. 12.

B. Finite-Volume Solution of Radiative Transfer Equations

The radiative field is assumed to instantaneously adjust to any changes in the flow-field. This is a consequence of radiative transport occurring at time-scales (defined by the speed of light) which are much smaller than those for other hydrodynamic and chemical phenomenon. The steady-state radiative transfer equation (RTE) in

the direction $\boldsymbol{\Omega}$ through a non-scattering media is:

$$\boldsymbol{\Omega} \cdot \nabla I_\nu = J_\nu - \kappa_\nu I_\nu \quad (20)$$

where I_ν is the monochromatic light intensity for frequency ν . The opacity and emission values corresponding to this frequency are κ_ν and J_ν respectively. The first-order RTE along with the following boundary condition for domain-directed intensity at the walls of the spacecraft yields a well-posed solution:

$$I_\nu = J_\nu / \kappa_\nu \quad \text{if} \quad \boldsymbol{\Omega} \cdot \mathbf{n}_w > 0 \quad (21)$$

where \mathbf{n}_w is the unit vector normal to a given boundary and pointing into the domain. Similarly, the latent domain-directed radiative intensity at the cold farfield boundary is set to zero. The net heat flux at a given point in space can be computed by integrating monochromatic intensity over the entire solid angle and frequency space:

$$\mathbf{q}_{\text{rad}} = \int_{\nu_i}^{\nu_f} \oint_{4\pi} I_\nu \boldsymbol{\Omega} d\boldsymbol{\Omega} d\nu \quad (22)$$

A three-dimensional angularly resolved solution of the RTE requires discretization in both the spatial and angular domains. The discrete-ordinates method involves computing the RTE equations for a set of discrete directions, $\boldsymbol{\Omega}^m$. This allows angular integration to be approximated by a weighted vector sum of radiative intensities in these discrete directions to obtain the spatially varying net radiative flux (and its divergence):

$$\mathbf{q}_{\text{rad}} = \int_{\nu_i}^{\nu_f} \oint_{4\pi} I_\nu \boldsymbol{\Omega} d\boldsymbol{\Omega} = \int_{\nu_i}^{\nu_f} \sum_m w^m I_\nu^m \boldsymbol{\Omega}^m d\nu \quad (23)$$

The quadrature weight and radiative intensity associated with direction $\boldsymbol{\Omega}^m$ are denoted by w^m and I_ν^m . Lebedev's quadrature rules are employed to determine $\boldsymbol{\Omega}^m$ and the corresponding weights [56] which minimizes the number of directions required for exactly integrating a polynomial of a given order.

The different methods for solving the problem of radiative heat transfer in participating media can be broadly classified into: a) techniques based on ray tracing, such as the ray tracing method [57] and the Monte Carlo method [58]; b) and methods based on spatial discretization RTEs using the finite element [32, 59] and finite volume [30, 60, 61] approaches. The current unified non-equilibrium framework is aimed at interfacing with existing finite volume based CFD solvers such that radiation and flowfield calculations can be performed in a loosely coupled manner. Therefore, in the interest of greater compatibility a finite volume based spatial discretization is adopted for resolving the RTE as well. Equation 20 for direction $\boldsymbol{\Omega}^m$ and frequency ν is recast by integrating it over i^{th} computational cell:

$$\int_{\mathbf{S}^i} I_\nu^m \boldsymbol{\Omega}^m \cdot d\mathbf{S} = \int_{V^i} (J_\nu - \kappa_\nu I_\nu^m) dV, \quad I_\nu(\mathbf{x}, \boldsymbol{\Omega}^m) : I_\nu^m(\mathbf{x}) \quad (24)$$

Standard finite volume simplifications are introduced by approximating volume integral as the product between the value at cell center (\mathbf{x}_c^i) and the cell volume (ΔV^i), and surface integral as the summation over faces of the product between the face-centered values (at \mathbf{x}_k^i) and the corresponding areas ($\Delta \mathbf{S}_k^i$):

$$\sum_k I_\nu(\mathbf{x}_k^i, \boldsymbol{\Omega}^m) \boldsymbol{\Omega}^m \cdot \Delta \mathbf{S}_k^i = \{J_\nu(\mathbf{x}_c^i) - \kappa_\nu(\mathbf{x}_c^i) I_\nu(\mathbf{x}_c^i, \boldsymbol{\Omega}^m)\} \Delta V^i \quad (25)$$

The surface summation can be further split into incoming ($\boldsymbol{\Omega}^m \cdot \Delta \mathbf{S}_k^i < 0$) and outgoing ($\boldsymbol{\Omega}^m \cdot \Delta \mathbf{S}_k^i > 0$) components. The current work uses first-order upwinding (referred to as the step scheme in radiation literature [62]) with outgoing radiative intensities at different face-centers set equal to the cell-center values for the corresponding cells. This sequence of steps yields the following form for $I_\nu(\mathbf{x}_c^i, \boldsymbol{\Omega}^m)$:

$$I_\nu(\mathbf{x}_c^i, \boldsymbol{\Omega}^m) = \frac{\sum_{\forall k \ni \boldsymbol{\Omega}^m \cdot \Delta \mathbf{S}_k^i < 0} I_\nu(\mathbf{x}_k^i, \boldsymbol{\Omega}^m) |\boldsymbol{\Omega}^m \cdot \Delta \mathbf{S}_k^i| + J_\nu(\mathbf{x}_c^i) \Delta V^i}{\sum_{\forall k \ni \boldsymbol{\Omega}^m \cdot \Delta \mathbf{S}_k^i > 0} |\boldsymbol{\Omega}^m \cdot \Delta \mathbf{S}_k^i| + \kappa_\nu(\mathbf{x}_c^i) \Delta V^i} \quad (26)$$

Equation 26 when written for all computational cells represents a sparse system of linear equations. The original system can be solved more efficiently by performing

“mesh sweeps” [63, 64]. This involves identifying the sequence (referred to as the “advance-order list”) in which individual cells need to be accessed for a given direction such that I_ν^m for all upstream neighboring cells have already been ascertained. This allows I_ν^m for a given cell to be computed using the closed-form explicit expression outlined in Eq. 26. The mesh reordering process transforms the original system into a lower triangular system and solving Eq. 26 is then akin to performing forward substitution. This is also analogous to marching along a discretized line-of-sight (or a characteristic), starting from a boundary surface. A potential drawback with applying mesh reordering algorithms to unstructured meshes is the possibility of encountering regions of computational cells with circular dependencies. This can result in an incomplete advance-order list unless explicit measures are introduced for breaking ties borne out of this circular behavior. The current framework utilizes sub-iterations (comparable to the Gauss-Seidel method) to accurately calculate I_ν^m for meshes with such deficiencies [65].

C. Self-consistent radiation-flowfield coupling

Spontaneous emission based on radiative transitions from vibrational levels included in CO₂ bin u (upper) to vibrational levels in CO₂ bin l yields the following transition rate (analogous to bin-averaged rate coefficients for collisional processes in Eq. 10):

$$\bar{K}_{u-l}^{\text{em}} = \frac{\mathcal{M}_u}{\rho_u N_A} \int_{\nu_i}^{\nu_f} \frac{\hat{J}_\nu^{u-l}}{h_P \nu} 4\pi d\nu \quad (27)$$

where \hat{J}_ν^{u-l} is the emission coefficient for transitions between vibrational bins u and l for frequency ν , and ρ_u and \mathcal{M}_u ($= \mathcal{M}_{\text{CO}_2}$) are the partial density and molar mass of u^{th} CO₂ vibrational bin. Radiative transitions in the opposite are driven by the absorption of the angularly/spectrally integrated radiative intensity at a given spatial

location:

$$K_{l-u}^{\text{ab}} = \frac{\mathcal{M}_l}{\rho_l N_A} \int_{\nu_i}^{\nu_f} \left(\frac{\hat{\kappa}_\nu^{l-u}}{h_P \nu} \oint_{4\pi} I_\nu d\Omega \right) d\nu \quad (28)$$

where $\hat{\kappa}_\nu^{l-u}$ is the absorption coefficient for transitions between vibrational bins l and u for frequency ν . The evaluation of K_{l-u}^{ab} for the line-by-line (LBL) approach is computationally challenging because of the dependence on non-local radiative intensity and the need to recompute absorption coefficients for individual transitions for all relevant frequency ranges. The current framework overcomes this problem through a combination of reduced-order models for thermochemistry and radiative properties and an efficient RTE solver based on finite volume and discrete ordinate methods. The resultant source terms arising from radiative transitions are added to the species continuity equation for the l^{th} CO_2 vibrational bin:

$$\dot{\omega}_{\text{rad}, \text{CO}_2}^b = \sum_{\forall u|u \neq l} \left(-K_{l-u}^{\text{ab}} \frac{\rho_l}{\mathcal{M}_l} + \bar{K}_{u-l}^{\text{em}} \frac{\rho_u}{\mathcal{M}_u} \right) \quad (29)$$

The following energy source term is obtained due to net radiative heating:

$$\Omega_{\text{rad}} = -\nabla \cdot \mathbf{q}_{\text{rad}} = -\nabla \cdot \int_{\nu_i}^{\nu_f} \oint_{4\pi} I_\nu \boldsymbol{\Omega} d\Omega d\nu \quad (30)$$

IV. HYDRODYNAMIC GOVERNING EQUATIONS

The original two-temperature (2-T) model [66] for species mass, mixture momentum, mixture total energy and vibrational-electronic energy conservation when augmented with the bin-based vibrational StS approach yield the following system of equations:

$$\partial_t \rho_i^b + \nabla \cdot [\rho_i^b (\mathbf{u} + \boldsymbol{\nu}_i^b)] = \mathcal{M}_i^b \dot{\omega}_i^b \quad (31)$$

$$\partial_t \rho_j + \nabla \cdot [\rho_j (\mathbf{u} + \boldsymbol{\nu}_j)] = \mathcal{M}_j \dot{\omega}_j \quad (32)$$

$$\partial_t (\rho \mathbf{u}) + \nabla \cdot (\rho \mathbf{u} \otimes \mathbf{u} + p \mathbb{I}) = \nabla \cdot \boldsymbol{\tau} \quad (33)$$

$$\begin{aligned}
\partial_t \rho \mathcal{E} + \nabla \cdot (\rho H \mathbf{u}) + \nabla \cdot \sum_i \sum_b \rho_i^b \boldsymbol{\nu}_i^b h_i^b + \nabla \cdot \sum_j \rho_j \boldsymbol{\nu}_j h_j \\
= \boldsymbol{\tau} : \nabla \mathbf{u} - \nabla \cdot \mathbf{q} + \Omega_{\text{rad}}
\end{aligned} \tag{34}$$

$$\begin{aligned}
\partial_t \rho e_V + \nabla \cdot (\rho e_V \mathbf{u}) + \nabla \cdot \sum_i \sum_b \rho_i^b \boldsymbol{\nu}_i^b e_{V,i}^b + \nabla \cdot \sum_j \rho_j \boldsymbol{\nu}_j e_{V,j} \\
= -\nabla \cdot \mathbf{q}_V + \Omega^{\text{CE}} + \Omega^{\text{VT}} + \Omega_{\text{rad}}
\end{aligned} \tag{35}$$

where symbol ∂_t is the partial time derivative $\partial/\partial t$. Species i for which a StS description is sought (CO₂ with a vibrational state-specific model in this study) is now replaced by b macroscopic bins. These bins are treated as pseudo-species in the gaseous mixture with their independent conservation equations. The net chemical production term $\mathcal{M}_i \dot{\omega}_i$ for individual bins includes all collisional ($\dot{\omega}_{\text{col},i}^b$ Eq. 10) and radiative ($\dot{\omega}_{\text{rad},i}^b$ from Eq. 29) processes considered in the StS model. Conversely, species j is still modeled in the conventional manner as a unitary entity with each internal mode described by only a single Boltzmann distribution. As a first approximation, no independent bin energy equations are solved in the current calculations and the total internal energy of bins is divided between the mixture translational-rotational and vibrational-electronic energies [67]. Thus, the conventional 2-T assumption is retained with translational energy states assumed to be in equilibrium at temperature T while vibrational and electronic modes are equilibrated at T_V . For the current reduced-order vibrational-specific StS model, this implies that vibrational states within individual bins are in localized Boltzmann distributions at T_V .

The contributions of individual species (and bins) is summed to yield mixture mass density ρ , mixture internal energy e , mixture enthalpy H , mixture total energy $\mathcal{E} = e + \frac{1}{2} \mathbf{u} \cdot \mathbf{u}$, and total pressure p . The total internal energy for b^{th} bin of species i is $[e_i^b = e_i^T(T) + e_i^R(T) + e_{i,b}^V(T_V) + e_i^E(T_V) + e_i^F]$, where the translational, rotational (rigid-rotor), electronic, and formation components are common

across a single species. However, vibrational energy is bin-specific because it is computed using partition functions based on the exact StS levels included in a given bin. Additionally, aggregate properties for species i (to be used with conventional 2-T modeling) are obtained by forcing the constituent bins into a single Boltzmann distribution [68]. Both bin-wise and Boltzmann-aggregate thermodynamic properties for species i are fitted using the NASA 9-coefficient polynomials [69], which are then directly evaluated during flowfield simulations.

Viscosity stress tensor $\boldsymbol{\tau}$ and conductive heat flux \mathbf{q} are modeled using Blottner viscosity fits [70] and the Eucken relation [71] with the Wilke mixing rule [72]. The diffusion velocities $\boldsymbol{\nu}_i$ obey Fick's law and are based on mixture-averaged diffusion coefficients [73]. Standard models are used for internal energy relaxation through vibration-translation energy transfer Ω^{VT} and chemistry vibrational-electronic coupling Ω^{CE} [74]. The Blottner viscosity coefficients and Millikan-White relaxation parameters of individual bins are currently set equal to the standard species model. This allows straightforward comparisons with state-of-the-art modeling approaches with a traditional 2-T flowfield being recovered in the absence of non-Boltzmann effects. The authors are currently involved in efforts to introduce separate bin energy equations which would allow bin temperatures to evolve independently of mixture T_V through StS inelastic energy transfer / chemical change processes (Eq. 11) and radiative transitions. The impact of detailed bin-specific transport properties (in contrast to using common Blottner viscosity fits and other simplifications) on aerothermal characteristics also needs to be ascertained in future studies. This would require developing rigorous formulations starting with approaches such as the Chapman-Enskog method [75, 76] and suitably modifying them to ensure compatibility with the MGME methodology [77]. The change in total mixture energy due to radiative heating is accounted for through Ω_{rad} in Eq. 30. This term is also included in the vibrational-electronic energy equation on account of radiative transitions occurring

between CO₂ vibrational levels.

V. RESULTS

The new reduced-order state-specific non-equilibrium framework has been used to improve predictive capabilities of the US3D code [37–39]. US3D solves the Navier-Stokes equations on unstructured grids using implicit data-parallel line-relaxation based on upwind numerical flux functions. It has been used extensively to study a wide variety of hypersonic flow problems including afterbody wakes [39, 78–81]. The standard Mars gaseous mixture comprising of five species – CO₂, CO, O₂, C and O – is considered in the present analysis [82]. The StS calculations replace CO₂ with 10 vibrational bins, which provides an optimal trade-off between accuracy and computational speed, while all other species are treated conventionally.

Absorption/emission spectra and subsequent radiative transfer calculations are performed using the non-equilibrium radiation (NERO) library [83]. This library is being developed by the authors to analyze complex three-dimensional radiative fields at reduced computational outlays by incorporating efficient numerical discretization techniques for RTEs and reduced-order modeling in the frequency space. The three main bands for CO₂ IR radiation – 1.5 μm , 2.7 μm and 4.5 μm – are considered in the present work. The smeared band technique is used to formulate band-wise spectral models, each comprising of 1000 frequency points. A total of 170 discrete quadrature directions and 10 sub-iterations are found to be sufficient for accurately modeling the radiation field around typical afterbody geometries. The finite-volume based RTE solver has been verified using canonical test cases such as radiative transfer inside a sphere with prescribed temperature profiles [84]. Additionally, afterbody surface radiative heat flux estimates obtained using NERO for the conventional 2-T flowfield are in excellent agreement with previous studies based on detailed line-by-

line models and ray-tracing calculations [1, 4]. The flowfield solution is accessed by NERO after a pre-defined number of iterations (set to 5,000 for this study). This information is used to update the spectral properties and re-compute spatially resolved, angularly integrated radiative intensity. Furthermore, in coupled mode, the volumetric radiative source terms for both species and energy (Eq. 30) equations are determined and then passed on to the flow solver.

A. Simulation Methodology

The present work is aimed at characterizing the interactions between flow structures, thermochemistry, and radiation for the Mars 2020 vehicle [1]. The upstream flow conditions are: $V_\infty = 3.9$ km/s, $\rho_\infty = 1.84 \times 10^{-3}$ kg/m³, and angle-of-attack in the $x - z$ plane $\alpha = 15.8$ deg. These conditions correspond to the trajectory point at $t = 91.5$ s and result in high backshell radiative heat flux as identified by previous studies based on tangent slab calculations. Supersonic inflow and outflow conditions are imposed on the outer periphery of the flow-domain. The surface of the spacecraft is assumed to be a no-slip, isothermal ($T_{\text{wall}} = 523$ K), super-catalytic wall. The super-catalytic boundary condition, as outlined in [85], is a conservative limiting case for design purposes when not modeling exact finite-rate surface reactions. It assumes that the gaseous mixture is forced back to its freestream composition and the available mixture chemical enthalpy is entirely reclaimed at the wall. This approximation has been widely used in aerothermal analysis of previous Martian missions such as Mars Exploration Rover (MER), Phoenix, and Mars Science Laboratory (MSL). The flowfield is assumed to be laminar and no special turbulence models are employed for the present work.

The computational mesh for the current study is illustrated in Fig. 6. Certain features, such as a sharp step between the heatshield-backshell juncture, which were

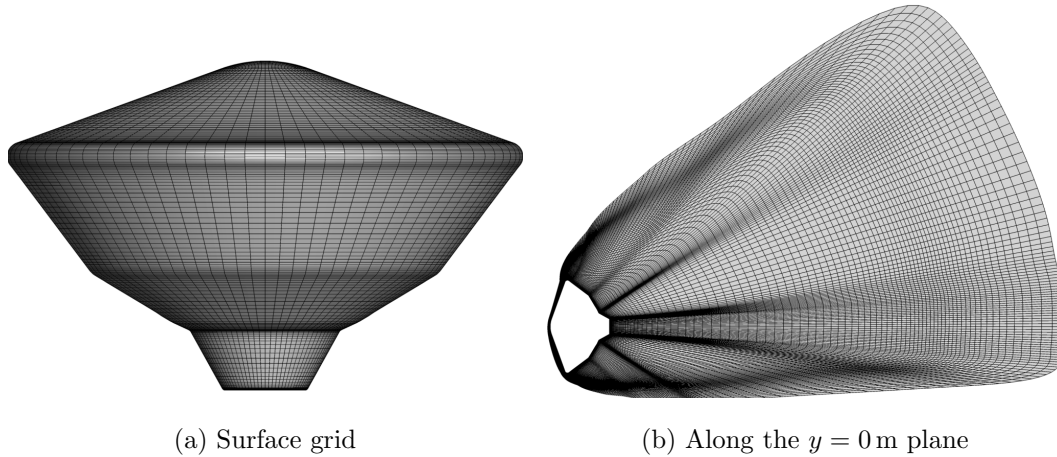


FIG. 6: Computational mesh for modeling the Mars 2020 wake flow.

present in the original outer mold line of the Mars 2020 capsule have been simplified in the interest of reducing simulation complexity. The resultant point-matched, multiblock structured mesh comprises of 1,740,800 volumetric elements and 13,600 elements on the vehicle surface. The original mesh has also been tailored at the outer grid boundary while clustering off-wall normal cells to allow sufficient resolution of the bow shock and boundary layer. Additional details on grid generation, element distribution, and mesh convergence for the Mars 2020 afterbody environment can be found in [1, 86].

Aerothermodynamic simulation best practices favored by previous work on afterbody heating for Mars 2020 and Mars Science Laboratory missions [1] have been adopted to obtain statistically converged flowfield and surface results. This involves first converging the forebody flowfield and then performing unsteady calculations with global time-stepping while computing running means of afterbody surface heat flux. The flowfield is considered to be converged once the change in the running means is below a certain threshold. All subsequent analysis is then performed on

the mean flowfield and the resultant radiation transfer phenomenon. It should be noted that the variance in surface heating is less than 0.5% for all cases presented in this work. Three sets of simulations are compared – first using the conventional 2-T Boltzmann approach (decoupled from radiation), next based on the reduced-order state-specific thermochemistry model (decoupled from radiation), and lastly with coupled reduced-order thermochemistry and radiation.

B. Decoupled Radiation

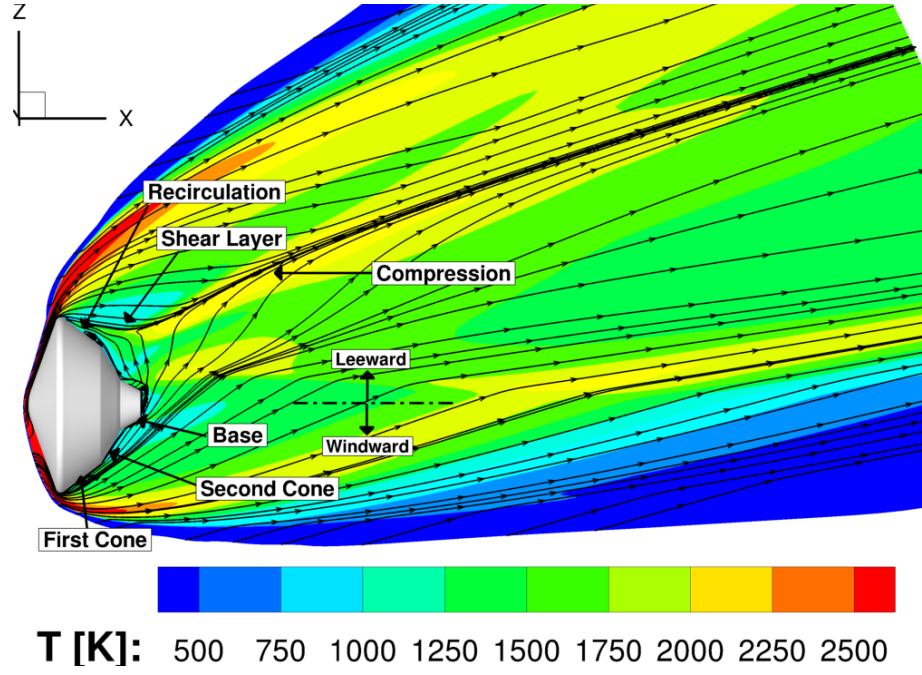
1. Flow Phenomenology

This section compares the difference in flowfield characteristics for the conventional 2-T and the ten bin-based StS approaches. Figure 7 presents the distribution of the translational-rotational temperature T , vibrational-electronic temperature T_V , and total CO_2 mass-fraction Y_{CO_2} along the $y = 0$ m plane. Individual streamlines and lines-of-sight (LOSs) for analyzing the evolution of flowfield and radiative intensity are also outlined. The typical dynamics of wake flows are clearly captured through the flow streamlines in Fig. 7a. A detached bow shock is formed ahead of the spacecraft which rapidly converts kinetic energy into internal energy resulting in a sharp increase in temperature and the onset of thermochemical non-equilibrium. The strength of the shock, characterized by the sudden change in properties across it, diminishes as it stretches downstream of the vehicle. The flow undergoes rapid expansion as it travels around the shoulder. The rapidity with which this temperature / pressure change occurs and the likelihood that the flow would be “frozen” in a state of non-equilibrium decreases as distance from the spacecraft surface increases. Despite this drop in temperature, the flowfield continues to be dominated by CO, O, and O_2 due to the large characteristic time-scales for CO_2 recombination [87].

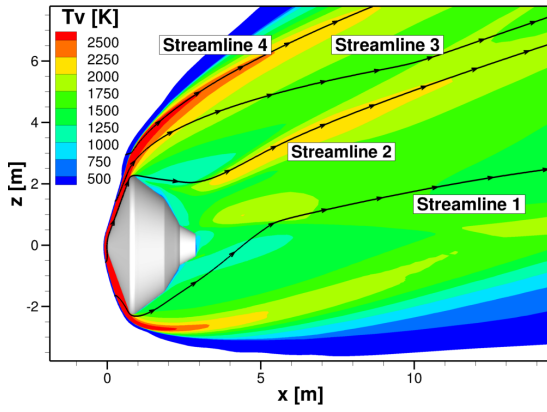
Viscous and pressure forces (which dominate inertial forces in the near-wake region) together result in the boundary layer originating from the vehicle surface separating and forming a free shear layer. A combination of viscous effects and an adverse pressure gradient in the immediate vicinity of the vehicle results in the flow past the shoulder eventually separating and forming a recirculation region. Since, the current simulation has been performed for $\alpha = 15.8$ deg, the system of rotating vortices typifying this region are no longer symmetric. Instead, the delay in separation on the windward side results in the recirculation region being skewed towards the leeward side with large vortices on the leeward first cone and the base and smaller vortices near the windside second cone. Further downstream the flow turns into itself and undergoes compression upon reaching the outer wake. The asymmetry due to a non-zero angle of attack also induces higher angles of deflection for streamlines moving from the windward side to the leeward side and results in stronger compression shocks and higher temperatures on the leeward side.

2. *Non-Boltzmann Thermochemistry*

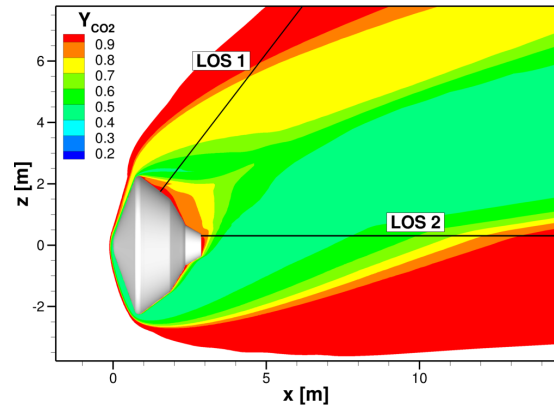
The trajectory profile for Mars entry is characterized by relatively low freestream velocities. Consequently, the conventional 2-T model, barring narrow isolated zones around the bow shock and the shoulder, yields similar predictions for both T and T_V . This behavior has also been observed in previous studies focusing on wake flows during Mars entry [4, 88]. Minimal differences in T and T_V values further underpins the fact that conventional multi-temperature models fail to sufficiently resolve non-equilibrium effects stemming from complex thermal relaxation mechanisms and non-Boltzmann state population distributions. Figure 8 compares predictions for the translational-rotational temperature T obtained using the bin-based StS and 2-T models. The percentage difference between quantities of interest from the two ap-



(a) Translational-rotational temperature T



(b) Vibrational-electronic temperature T_V



(c) Total CO_2 density

FIG. 7: Distribution for T , T_V , and ρ_{CO_2} along the $y = 0$ m plane for the 10 bin-based StS model. Individual streamlines and LOSs for analyzing flowfield and radiative intensity respectively are also defined.

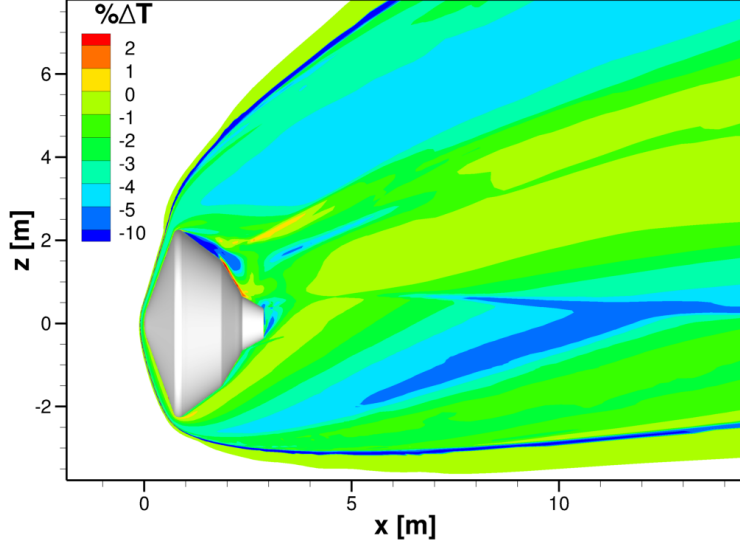


FIG. 8: Percentage difference in predicted translational-rotational temperature T between bin-based StS and 2-T models: $(T^{\text{StS}} - T^{2\text{-T}}) / T^{2\text{-T}} \times 100\%$.

proaches is computed as: $(Q^{\text{StS}} - Q^{2\text{-T}}) / |Q^{2\text{-T}}| \times 100\%$. Similarly, the difference in partial densities of CO_2 vibrational bins 1, 2, 5, and 8 are presented in Fig. 9. The corresponding bin-wise properties for the conventional 2-T model are obtained as a post-processing step by assuming that CO_2 vibrational states lie on a Boltzmann distribution at T_V . StS modeling in an ideal chemical reactor (summarized in Section II B) allows a rough interpretation of non-equilibrium dynamics for wake flows. The first three bins reach Boltzmann distribution at $t = 10^{-4}$ s (\sim average flow transit time) once the reactor is suddenly cooled. The high energy states (> 1.5 eV) on other hand are overpopulated and form a complex non-Boltzmann comb-like structure which is equilibrated only at $t \sim 10^1$ s. This disparity in equilibration time scales is also observed Fig.9, with partial density estimates varying by multiple orders of magnitude between the StS and 2-T approaches for the upper bins. The difference for the first three bins, which represent about 99% of all CO_2 molecules, is signifi-

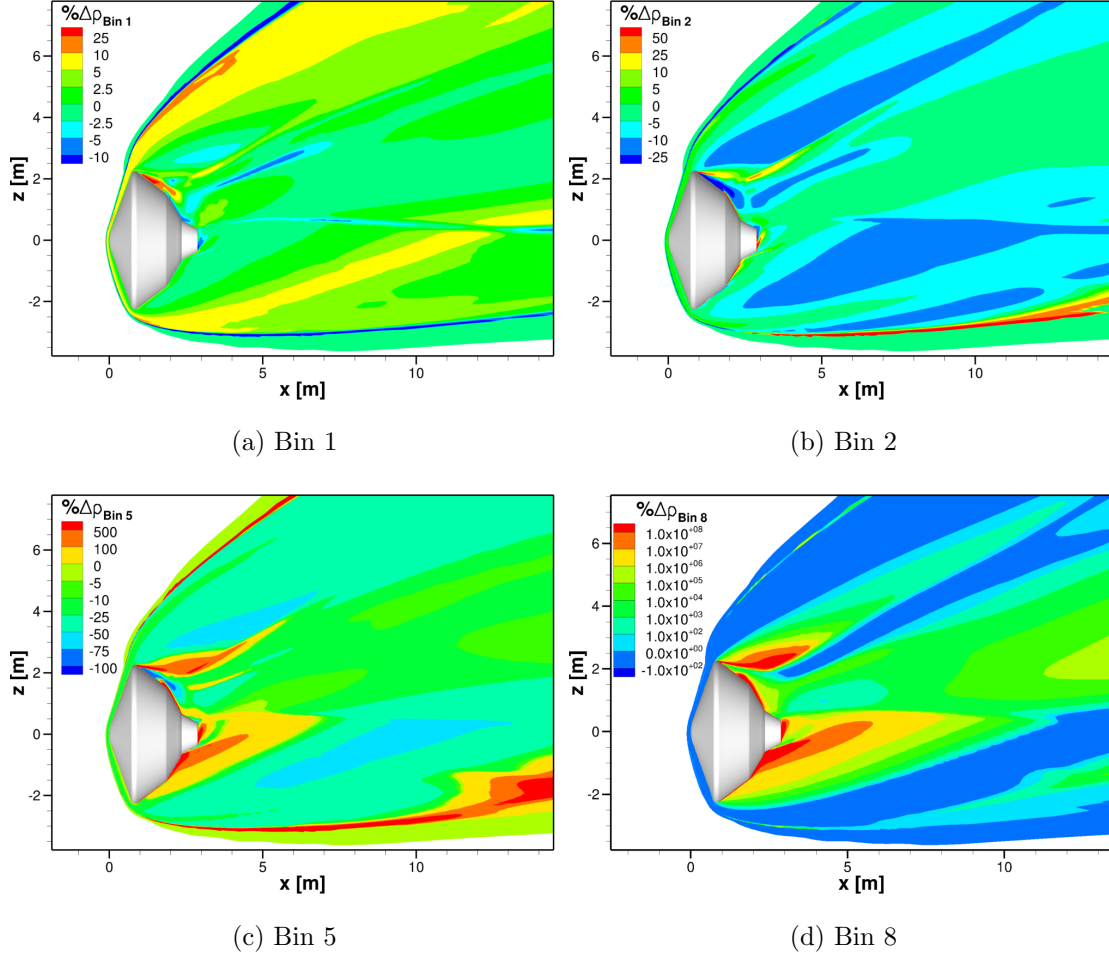


FIG. 9: Percentage difference in predicted partial densities of CO_2 vibrational bins 1, 2, 5, and 8 between bin-based StS and 2-T models: $(\rho_{bin}^{\text{StS}} - \rho_{bin}^{2\text{-T}}) / \rho_{bin}^{2\text{-T}} \times 100\%$.

cantly lower. Thus, the sparsely populated upper bins have minimal impact on the bulk T (which also includes contributions from other mixture species) and despite their strongly non-Boltzmann behavior $|\% \Delta T| < 4\%$ for most of the afterbody.

The streamlines defined in Fig. 7b are characterized by different rates at which the flow expands while traveling around the shoulder to the afterbody region rang-

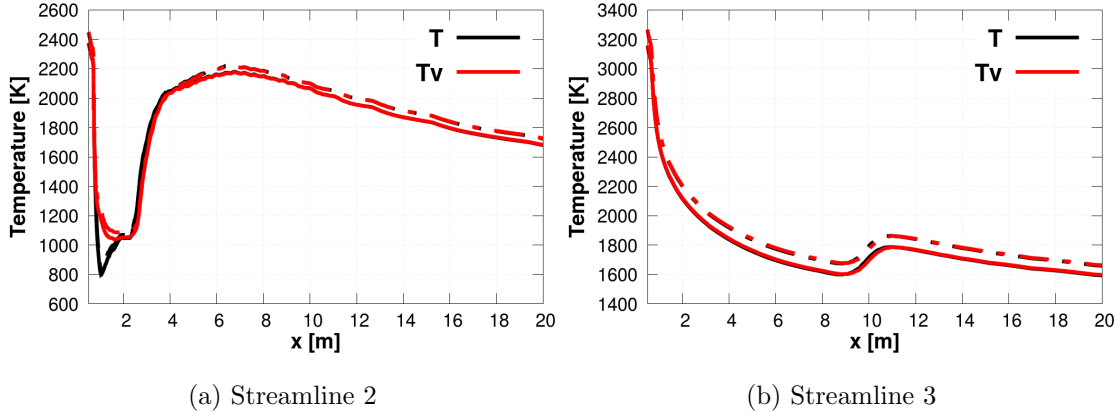


FIG. 10: Distribution of T (black) and T_V (red) along streamlines 2 and 3. Solid and dashed lines represent bin-based StS and conventional 2-T models respectively.

ing from streamlines 1 and 2 that experience “freezing” in the near-wake region to streamline 4 which completely skips the core viscous wake and experiences no concomitant expansion after the oblique shock. Figure 10 highlights the variation in rate of expansion and the subsequent recovery due to compression along streamlines 2 and 3. It is clear that both T (black) and T_V (red) match each other except for a narrow region around the shoulder. Additionally, T and T_V values computed using the bin-based StS (solid) model are slightly lower than those for the conventional 2-T (dashed) model. Bin densities for both bin-based StS (solid) and 2-T (dashed) models along the four streamlines are plotted in Fig. 11. A simple rule of thumb for the reduced-order model is that a higher density value corresponds to a lower bin index. A common theme for all four streamlines is the limited dissimilarity between results for the first four bins which constitute the lower end of the state population distribution. On the contrary, partial densities for the last four bins differ by almost nine orders of magnitude. Low number densities and temperatures during expansion severely restricts thermal relaxation and renders the state population distribution

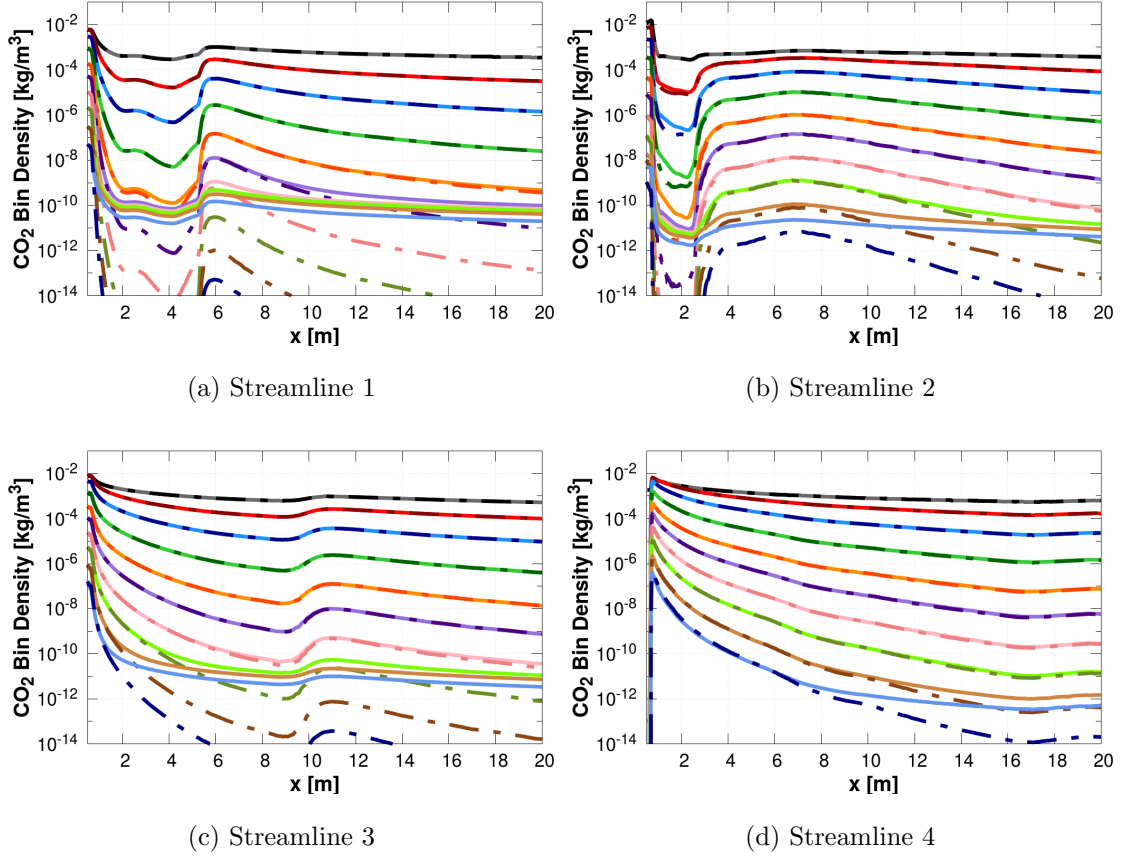


FIG. 11: Partial densities of CO_2 vibrational bins along different streamlines. Solid and dashed lines represent bin-based StS and conventional 2-T models respectively.

unable to respond to changes in flow conditions. This behavior is particularly pronounced for the upper bins with high characteristic relaxation times, resulting in the conventional 2-T model under-predicting bin populations due to the assumption of instantaneous equilibration at T_V . It is interesting to note that relaxation time-scales for the last two bins are so large that non-equilibrium behavior is induced even in streamline 4 once the flow has moved sufficiently away from the high temperature region around the bow shock. A non-Boltzmann factor to quantify deviation from a

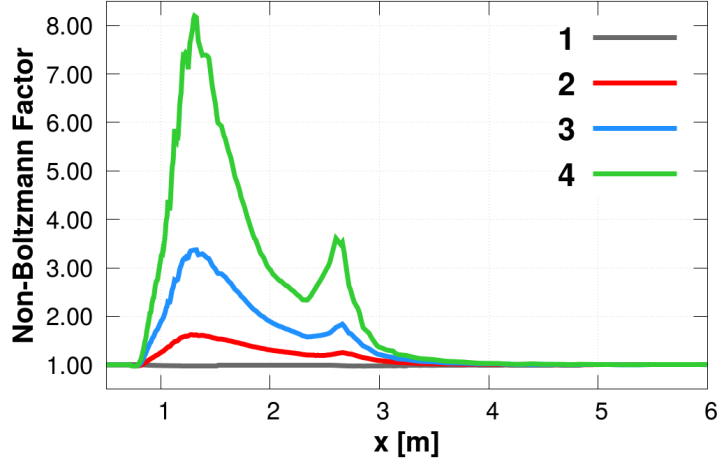
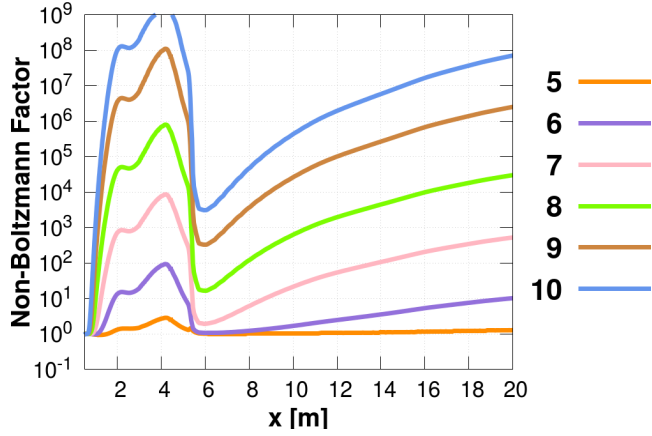


FIG. 12: Non-Boltzmann factor (Eq. 36) for CO₂ vibrational bins 1 to 4 along streamline 2.

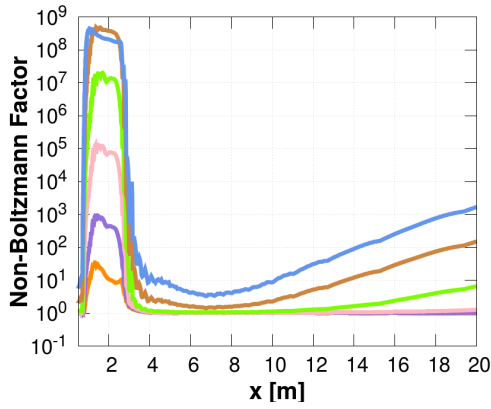
Boltzmann state population distribution for the i^{th} bin can be defined as:

$$NB_i = \rho_i / \rho_i^{\text{Bol}} \quad (36)$$

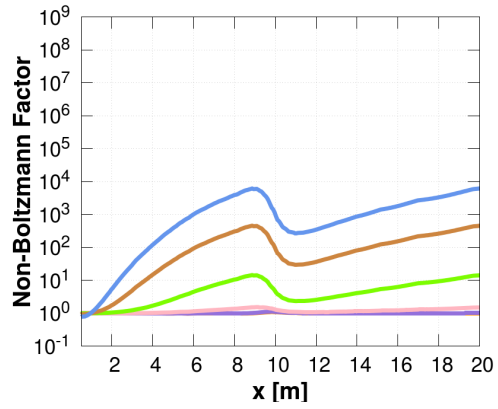
where ρ_i the bin density obtained directly from the reduced-order StS simulation and ρ_i^{Bol} is the corresponding bin density based on a Boltzmann distribution at T_V and total CO₂ density ρ_{CO_2} from the same simulation. The non-Boltzmann factor for the first four bins remains close to 1 except for the strong expansion region near the shoulder of the spacecraft (Fig 12). The strong non-equilibrium experienced by the upper bins is illustrated in Fig. 13 with NB_i for different bins ranging between 10^1 and 10^9 . The increasing distance from the vehicle surface and easing rate of expansion between streamlines 1 and 3 allows thermalization to proceed further and reduces the peak value of NB_i from 10^9 to 10^4 . Non-Boltzmann effects persist longer along streamline 1 on the windward side as compared to streamline 2 on the leeward side (as evidenced by figures 11 and 13) despite more rapid expansion and a



(a) Streamline 1



(b) Streamline 2



(c) Streamline 3

FIG. 13: Non-Boltzmann factor (Eq. 36) for CO_2 vibrational bins 5 to 10 along different streamlines.

larger re-circulation zone on the leeward side. This is a direct consequence of weaker recompression and lower temperature recovery on the windward side which reduces the collision rates and retards equilibration.

3. Radiative Transfer

Although the current framework computes the three-dimensional angularly integrated radiation field, it is still instructive to compare flowfield properties and the resultant radiative intensity along individual LOSs for the two approaches. The two LOSs outlined in Fig. 7c are normal to the first cone and the base of the afterbody on the leeward side. A parameter called flow factor F_{i-j} is defined which attempts to condense the impact of bin densities, T_V , and degree of non-Boltzmann behavior on radiative transitions between the i^{th} and j^{th} bins for frequency ν into one convenient term:

$$F_{i-j} = \rho_i \frac{NB_j}{NB_i} \exp\left(\frac{-h_P \nu}{k_B T_V}\right) \quad (37)$$

where h is the Planck's constant, k_B is the Boltzmann constant, and ρ_i is bin density either obtained directly from the reduced-order StS simulation or post-processed in the case of conventional 2-T modeling. The flow factor term appears in the expression for absorption κ_ν^{i-j} and J_ν^{i-j} emission coefficients for a given bin pair (equations 18 and 19):

$$\hat{\kappa}_\nu^{i-j} = \frac{\sigma_\nu^{i-j}}{N_A} (\rho_i - F_{i-j}) \quad (38)$$

$$\hat{J}_\nu^{j-i} = \frac{\sigma_\nu^{i-j}}{N_A} \frac{2h_P \nu^3}{c^2} F_{i-j} \quad (39)$$

where σ_ν^{i-j} is the absorption cross-section at ν , N_A is the Avogadro's number, and c is the speed of light. A larger value of F_{i-j} implies more emission and less absorption emanating from radiative transitions between bin pair $i - j$ and would increase radiative intensity along a LOS. In order to simplify the flow factor analysis, ν is set equal to the frequency at the middle of the dominant $4.5 \mu\text{m}$ band. Figure 5 indicates that emission coefficients per unit bin density for radiative transitions between bin pairs $1 - 1$, $2 - 1$, $2 - 2$, $3 - 2$, $3 - 3$, $4 - 3$, and $4 - 4$ are comparable. However,

the partial densities of the first two bins are much larger compared to the remaining bins. Flow factors and resulting radiative emissions from transitions involving these two bins are significantly higher as well. Thus, IR radiation for the afterbody region is shaped entirely by the characteristics of bin 1 and to a lesser extent bin 2.

Figure 15 presents the variation in temperatures (both T and T_V with solid and dashed lines corresponding to bin-based StS and conventional 2-T models respectively), percentage difference in flow factors, and total radiative intensity along the two LOSs. The total radiative intensity for the first LOS reaches $\sim 90\%$ of its peak value approximately 5 m from the wall surface. This location is marked as a white dot in Fig. 16 which also presents the percentage different in total CO_2 density between bin-based StS and 2-T models. Figure 16 indicates the rise in radiative intensity occurs almost exclusively in a region bounded by the bow shock and streamline 4 which comprises of dissociating flow that undergoes no expansion. Kustova *et al.* [13] have previously shown that conventional 2-T modeling overpredicts the rate of dis-

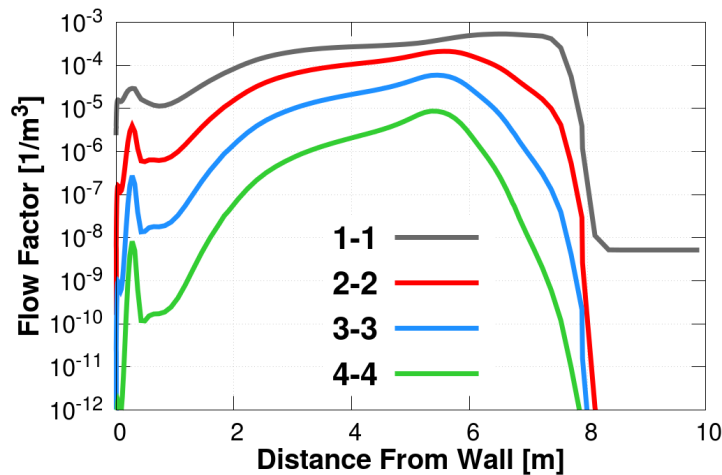
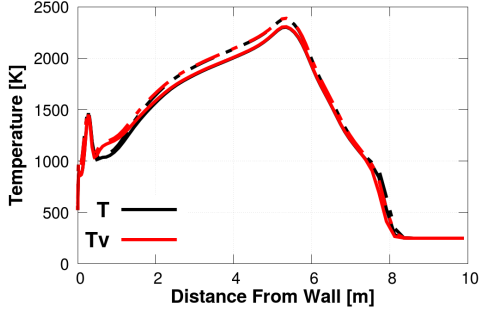
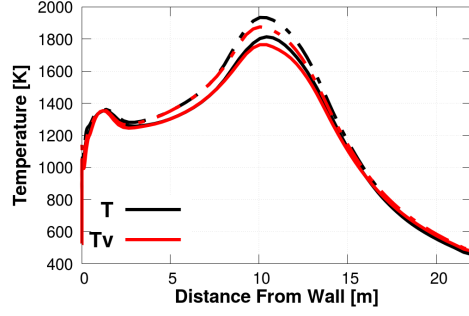


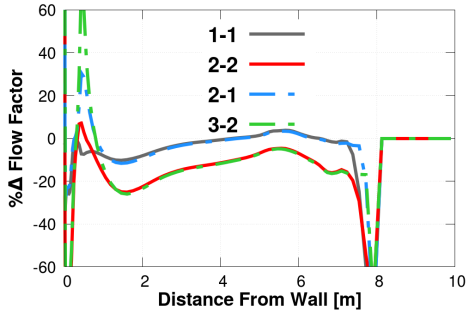
FIG. 14: Flow factors (Eq. 39) for the first four CO_2 vibrational bins along LOS 1.



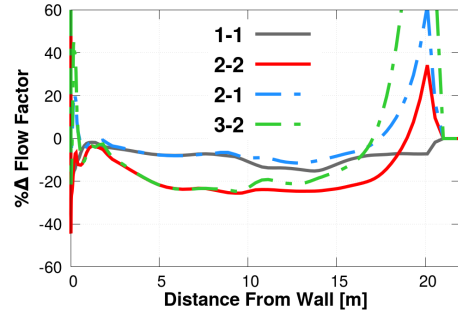
(a) Temperatures - LOS 1



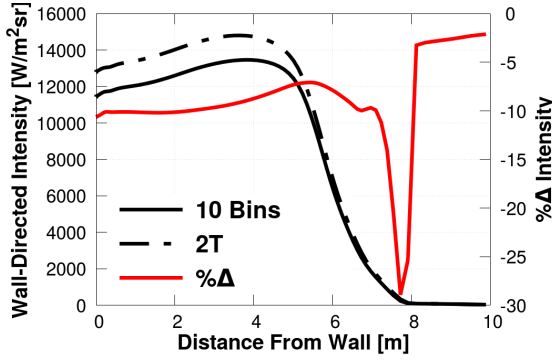
(b) Temperatures - LOS 2



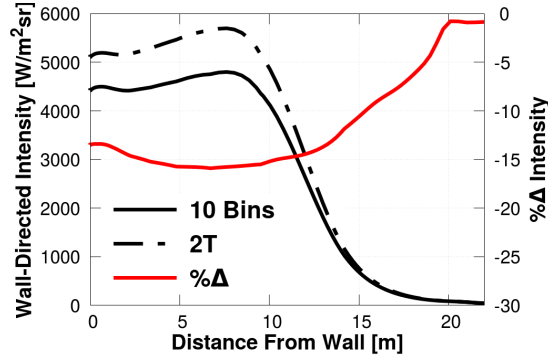
(c) $\% \Delta F_{i-j}$ - LOS 1



(d) $\% \Delta F_{i-j}$ - LOS 2



(e) Radiative intensity - LOS 1



(f) Radiative intensity - LOS 2

FIG. 15: Temperatures - T and T_V (solid and dashed lines correspond to bin-based StS and conventional 2-T models respectively), $\% \Delta F_{i-j}$, and total radiative intensity along different LOSs. Percentage difference is computed as:

$$\frac{(Q^{\text{StS}} - Q^{2\text{-T}})}{|Q^{2\text{-T}}|} \times 100\%.$$

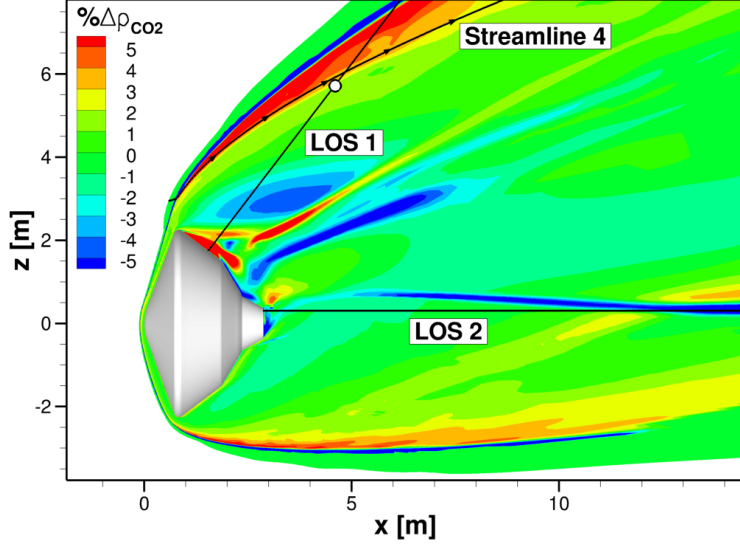


FIG. 16: Percentage difference in total CO_2 density between bin-based StS and 2-T models: $(\rho_{\text{CO}_2}^{\text{StS}} - \rho_{\text{CO}_2}^{2\text{-T}}) / \rho_{\text{CO}_2}^{2\text{-T}} \times 100\%$.

sociation when compared to the current StS model. Thus, $\% \Delta \rho_{\text{CO}_2} > 0$ and T (and T_V) is lower (one possible explanation being greater CO_2 results in larger mixture heat capacity) for the bin-based StS model. This trend is reversed in the case of the second bin, with partial density (Figure 9) being smaller due to lower T_V . The two competing effects of higher density and lower temperature characterizing the first bin appear to cancel each other out with $\% \Delta F_{1-1}$ being only slightly negative. Conversely, $\% \Delta F_{2-2}$ has a more pronounced negative value due to both density and temperature effects reinforcing each other. It should be noted that $\% \Delta F_{2-1}$ and $\% \Delta F_{3-2}$ follow $\% \Delta F_{1-1}$ and $\% \Delta F_{2-2}$ respectively except for the recirculation region where non-equilibrium effects dominate. The utility of analyzing local radiative behavior using flow factors is evident in Fig. 15, with changes in $\% \Delta I$ mirroring the behavior of $\% \Delta F_{i-j}$. The percentage difference in radiative intensity at the wall is approximately the weighted mean value along the LOS of $\% \Delta F_{i-j}$ for the dominant

bin-pairs. The same behavior borne out of slower dissociation for the StS approach is seen along the middle-section of LOS 2. Crucially, non-Boltzmann effects are more pronounced further into the viscous wake (~ 12 m onwards) which results in F_{i-j} being higher for the StS model. An important conclusion that can be drawn from this analysis is that radiative energy emanating from the bow shock is much higher compared to the rest of the wake.

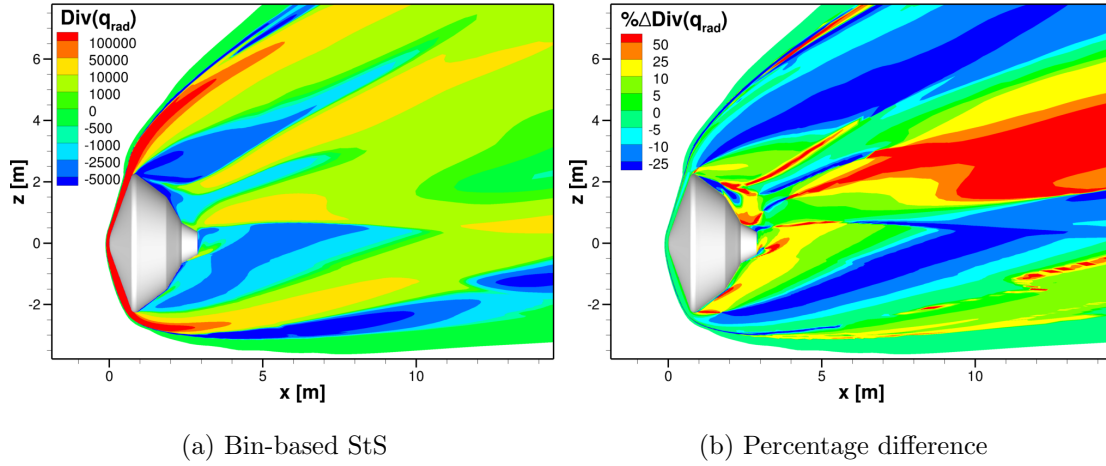


FIG. 17: Negative value of volumetric radiative heating term. Percentage difference computed as: $(\nabla \cdot \mathbf{q}_{\text{rad}}^{\text{StS}} - \nabla \cdot \mathbf{q}_{\text{rad}}^{2-T}) / |\nabla \cdot \mathbf{q}_{\text{rad}}^{2-T}| \times 100\%$ (right).

Figure 17 presents divergence of the total radiative heat flux $\nabla \cdot \mathbf{q}_{\text{rad}}$ along the $y = 0$ m plane for the bin-based StS simulation and the percentage difference between the two models. A positive (negative) value for $\nabla \cdot \mathbf{q}_{\text{rad}}$ indicates that the flow at a particular location is a net emitter (absorber) of radiative energy and adds to the radiative heat flux received by the vehicle. The consistently high magnitude of the $\nabla \cdot \mathbf{q}_{\text{rad}}$ term associated with the hot dissociating flow after the oblique shock further confirms that radiative surface heat flux is dominated by the properties of this small section of the flowfield. Figure 18 compares the total radiative heat flux received by

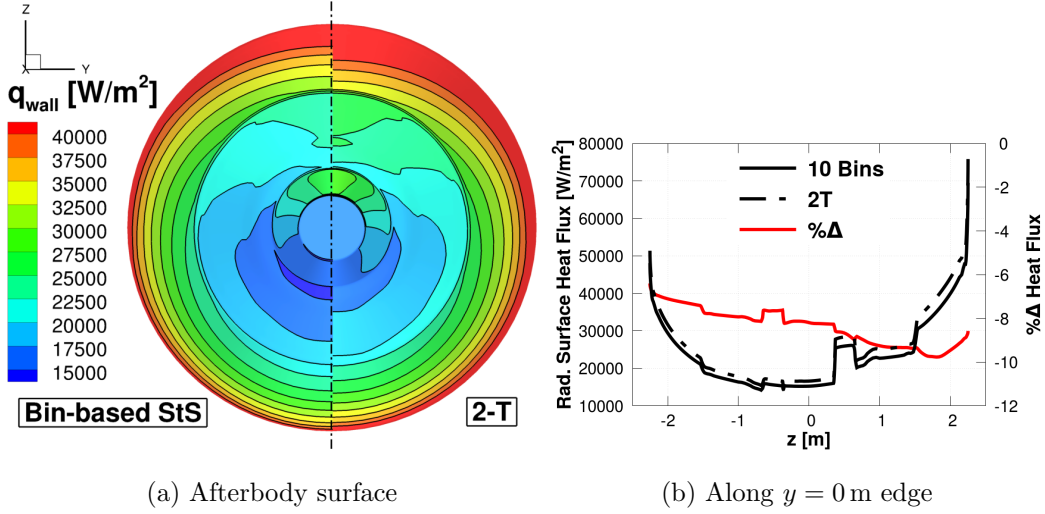


FIG. 18: Total radiative surface heat flux q_{wall} from bin-based StS and 2-T models. Percentage difference computed as: $(q_{\text{wall}}^{\text{StS}} - q_{\text{wall}}^{\text{2-T}}) / q_{\text{wall}}^{\text{2-T}} \times 100\%$

the afterbody and the difference between the two approaches along the $y = 0$ m edge. The conventional 2-T model clearly overpredicts surface heat flux which is in line with our previous analysis. It is interesting to note that percentage difference in estimates for incident radiative flux continues to hover around the same value as $\% \Delta I$ at the wall for LOS 1 and $\% \Delta (\nabla \cdot \mathbf{q}_{\text{rad}})$ near the bow shock region. The enclosed expanding wake despite experiencing significant non-Boltzmann behavior (resulting in higher $\% \Delta (\nabla \cdot \mathbf{q}_{\text{rad}})$ and $\% \Delta I$ for LOS 2) is rendered radiatively non-participating due to a significant drop in CO_2 density. Thus, its role in determining vehicle radiation characteristics is largely limited even for the base ($z \in [-0.37, 0.37]$ m) which has a comparatively smaller view factor with respect to the bow shock. Furthermore, unlike atomic radiation [21] the impact of non-Boltzmann effects on total CO_2 IR heating is further minimized due to the preponderance of radiative transitions within the ground vibrational bin which has a short thermal relaxation time period.

This also leads the authors to conclude that increasing the total number of vibrational bins would not appreciably change estimates for surface radiative flux. The dominant lower bins (although now more in number) would continue to remain in an equilibrium Boltzmann distribution, matching the behavior implicitly obtained through the 2-T model.

C. Coupled Radiation

Previous studies on earth entry flows with low density wakes [21] have indicated that radiative transitions outlined in Section III C can have a significant on the population of higher energy levels. Conventional techniques for coupling radiation to flow chemistry / thermal relaxation rely on the escape factor approximation [89] for computing reaction rate coefficients due to absorption K_{l-u}^{ab} . An escape factor parameter EF_{l-u} with a value between 0 (optically thick transitions) and 1 (optically thin transitions) is used to express K_{l-u}^{ab} as a fraction of the total spontaneous emission from a given location:

$$K_{l-u}^{\text{ab}} = (1 - EF_{l-u}) \bar{K}_{u-l}^{\text{em}} \frac{\rho_u}{\rho_l} \quad (40)$$

The escape factor EF_{l-u} is either prescribed a constant value [90] or computed solely on the basis of local properties at a given location [89]. Additionally, this approach is unable to model strong absorption of non-local emission because EF_{l-u} cannot be assigned negative values. The current framework eschews these simplifications in order to accurately assess the possible effects of absorption of non-local IR radiation emanating from surrounding flows. This is computationally prohibitive without the use of model-reduction techniques and apart from few exceptions involving atomic species [21, 58], has typically been avoided while studying complex three-dimensional flow problems. An exact value for EF_{l-u} is later computed as a post-processing step

using the detailed values of $\bar{K}_{u-l}^{\text{em}}$ and K_{l-u}^{ab} in order to gain useful insights into the coupling between local thermochemistry and the global radiative field:

$$EF_{l-u} = 1 - \frac{K_{l-u}^{\text{ab}} \rho_l}{\bar{K}_{u-l}^{\text{em}} \rho_u} \quad (41)$$

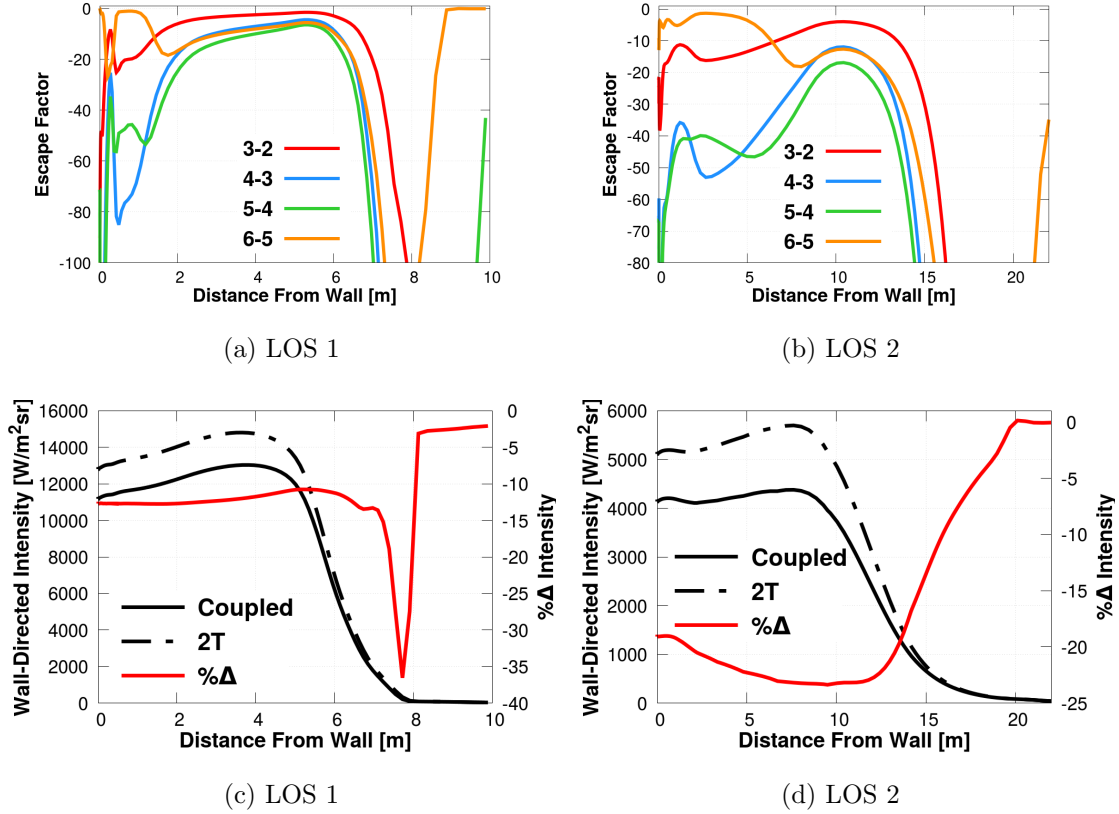


FIG. 19: Escape factor and total radiative intensity along different LOSs.

Percentage difference is computed as: $(Q^{\text{StS}} - Q^{2\text{-T}}) / |Q^{2\text{-T}}| \times 100\%$.

The escape factors for transitions involving the upper vibrational bins such as 3-2, 4-3, 5-4, and 6-5 along the two LOSs for 10 bins-based StS simulations with self-consistent non-local radiation coupling are outlined in Fig. 19. It should be noted that unlike approximate escape factor methods, the lower limit for escape factors is

not set to zero in the current study. Large negative values in Fig. 19 indicate that owing to the global radiation field (represented by the scalar integral $\oint_{4\pi} I_\nu d\Omega$ in Eq. 28), transition rates due to absorption are significantly higher than those due to emission. This results from photochemical transitions involving different CO₂ vibrational levels (or bins for the current reduced-order StS description) overlapping in the frequency space as outlined in Fig 5. Thus, emission by the dominant first bin becomes available for absorption by the upper bins. This radiative environment is fundamentally different from those for atomic species [91] where the underlying spectra largely consists of separated lines. However, as Fig. 14 and the subsequent analysis indicates that absorption/emission coefficients for the upper bins are smaller to those of the first bin by multiple orders of magnitude. Additionally, the characteristic radiative intensity for Martian missions is lower than those for Earth-return profiles due to the large difference in entry speeds. Consequently, there is no significant repopulation of the upper bins and their contribution to total radiative emission remains minimal even for the coupled simulation. Moreover, lower radiative intensity also results in internal dynamics of the first two bins being dominated by collisional processes in the strongly emitting regions with radiative processes having a discernible impact only in the radiatively insignificant near-wake zone.

The energy source term from Eq. 30 has a more pronounced impact on total radiative heat flux. The majority of the flowfield barring the recirculation zone are net emitters of radiative energy (Fig. 17). This loss of energy results in a drop in temperature and subsequently, lowered spontaneous emissions. Thus, radiative intensities for StS simulations with radiative coupling are lower than those for the uncoupled StS and 2-T cases. A comparison between the total radiative surface heat flux along the $y = 0$ m edge obtained using the 2-T, uncoupled StS, and coupled StS simulations is presented in Fig. 20.

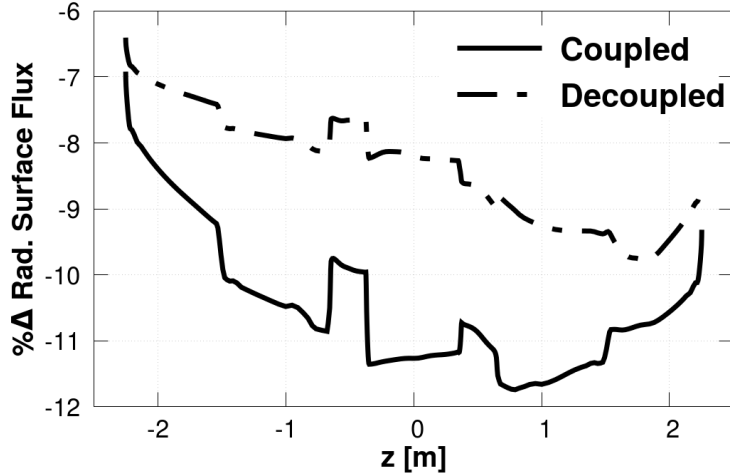


FIG. 20: Percentage difference in total radiative surface heat flux coupled/uncoupled bin-based StS and 2-T models along the $y = 0$ m edge:

$$(q_{\text{wall}}^{\text{StS}} - q_{\text{wall}}^{2\text{-T}}) / q_{\text{wall}}^{2\text{-T}} \times 100\%$$

VI. CONCLUSIONS

This work presents a simulation methodology for modeling non-equilibrium thermochemistry and radiative transfer in a unified manner for complex three-dimensional flow problems. The resultant simulation toolset is then employed with the US3D flow solver for characterizing CO_2 wake flows during planetary entry of the Mars 2020 vehicle. The combination of multi-group maximum entropy method and adaptive binning allows the non-Boltzmann state population distribution and resultant macroscopic properties to be computed accurately at significantly lowered costs. Thus, starting from a vibrational-specific CO_2 StS model, an equivalent reduced-order system with only 10-30 bins is synthesized. Similarly, self-consistent flow-coupled radiative transfer calculations are achieved by reducing computational overhead associated with spectral, angular, and spatial discretizations. These im-

provements in computational tractability allow flow source terms emanating from non-local absorption of radiative intensity to be consistently computed without resorting to traditional simplifications such as the tangent-slab method or local escape factor approximation.

Statistically converged solutions for hypersonic flows around the Mars 2020 vehicle are obtained using the conventional 2-T model and 10 bin-based StS model for CO₂ vibrational non-equilibrium. This includes both decoupled radiative calculations (by post-processing the final flowfield) and flow-radiation two-way coupled simulations. The translational-rotational temperature is found equal to the vibrational-electronic temperature for most of the flowfield which clearly indicates that non-Boltzmann deviations in vibrational state population distributions cannot be fundamentally accounted for through conventional multi-temperature approaches. Streamlines that pass through the near-wake region undergo rapid expansion resulting in the population of mid-lying and upper CO₂ vibrational levels being frozen. Bin-based StS approach captures this non-equilibrium behavior whereas the 2-T model by forcing thermal equilibration underpredicts the population distribution by multiple orders of magnitude. However, both ideal chemical reactor and flowfield simulations suggest that the lowest vibrational levels (bins 1 and 2) reach their final equilibrium state fairly rapidly. Hence, bulk properties such as temperature, density, and total CO₂ mass fraction do not differ significantly between the bin-based StS and 2-T approaches. An analysis of the resultant radiative transfer indicates that its dynamics are completely dominated by the ground vibrational levels (Bin 1) owing to their considerably higher number densities. Furthermore, radiative intensities along LOSs crossing the bow shock reach their final values exclusively in a narrow high density/temperature region around the shock that undergoes no discernible expansion. Thus, the impact of non-Boltzmann effects induced in near-wake flows on the total afterbody radiative heat flux is largely minimized. Nevertheless, surface heat flux

predicted by 2-T model is almost 10% greater due to higher post-shock temperatures. Coupled flow-radiation simulations accentuate the difference in surface flux estimates between the two approaches to a slightly higher 12%. Non-local absorption (negative escape factors) of radiative energy emitted by the shock result in re-population of the higher levels in the wake. But, lower Martian entry speeds (less total radiative intensity) and the dynamics of ground vibrational levels still being informed by collisional processes restricts the overall influence of flow-radiation coupling.

The current work provides a cost-effective modular framework that can be applied to the study of any non-equilibrium dominated problem ranging from hypersonic planetary entry (Lunar-return, Titan entry) or low-temperature plasmas in material processing and manufacturing. To that end, the validity of StS models and LBL radiation databases have a strong bearing on the accuracy of the current reduced-order thermochemistry and spectral properties respectively. The current work relies on a vibrational-specific description of CO₂ that is derived using modified-SSH theory and legacy experimental data. Conventional multi-temperature models for thermochemical non-equilibrium also attempt to reproduce these experimental results. This common reliance could explain the limited contrast between the current 2-T and bin-based StS predictions. Research is being currently performed to develop CO₂ StS model from first-principle quantum chemistry calculations [87] that can introduce two key improvements: a) eliminate selective vibrational transitions that are an artifact of extrapolating low energy rates through SSH theory, and b) correctly replicate CO₂ recombination which involves a transient electronically-excited triplet state being formed from ground CO and O and then decaying to the ground singlet state CO₂(X¹Σ_g⁺). The results from this study will be revisited in the future once these ab-initio rates for CO₂ become available. Additionally, the authors plan to perform detailed comparisons with data for the Mars afterbody radiative environment obtained from both ground-based facilities [5, 92] and free-flight measurements [93] in

future studies.

ACKNOWLEDGMENTS

This research has been supported under a NASA Early Career Faculty Award (grant number NNX15AU4-4G). The authors are grateful to Prof. Elena Kustova and Dr. Iole Armenise for their assistance with the CO₂ state-to-state model.

-
- [1] A. Wise, D. K. Prabhu, C. O. Johnston, D. A. Saunders, and K. T. Edquist, Computational aerothermodynamic environments for the mars 2020 entry capsule, AIAA Paper , 3116 (2018).
 - [2] P. A. Gnoffo, Planetary-entry gas dynamics, Annual Review of Fluid Mechanics **31**, 459 (1999).
 - [3] S. T. Surzhikov, Comparative analysis of radiative aerothermodynamics of Martian entry probes, AIAA Paper , 2867 (2012).
 - [4] A. M. Brandis, D. A. Saunders, C. O. Johnston, B. A. Cruden, and T. R. White, Radiative heating on the after-body of Martian entry vehicles, AIAA Paper , 3111 (2015).
 - [5] H. Takayanagi, A. Lemal, S. Nomura, and K. Fujita, Measurement of carbon dioxide infrared radiation in the afterbody of a Mars entry capsule, AIAA Paper , 1369 (2017).
 - [6] T. K. West, J. Theisinger, A. J. Brune, and C. O. Johnston, Backshell radiative heating on human-scale Mars entry vehicles, AIAA Paper , 4532 (2017).
 - [7] C. Park, J. T. Howe, R. L. Jaffe, and G. V. Candler, Review of chemical-kinetic problems of future NASA missions. II-Mars entries, Journal of Thermophysics and Heat transfer **8**, 9 (1994).

- [8] M. Panesi, A. Munafò, T. E. Magin, and R. L. Jaffe, Nonequilibrium shock-heated nitrogen flows using a rovibrational state-to-state method, *Physical Review E* **90**, 013009 (2014).
- [9] K. L. Heritier, R. L. Jaffe, V. Laporta, and M. Panesi, Energy transfer models in nitrogen plasmas: Analysis of $N_2(X^1\sigma_g^+) - N(^4S_u) - e^-$ interaction, *The Journal of Chemical Physics* **141**, 184302 (2014).
- [10] A. Sahai, B. Lopez, C. O. Johnston, and M. Panesi, A reduced order maximum entropy model for chemical and thermal non-equilibrium in high temperature CO_2 gas, *AIAA Paper* , 3695 (2016).
- [11] R. L. Jaffe, D. W. Schwenke, and G. Chaban, Theoretical analysis of N_2 collisional dissociation and rotation-vibration energy transfer, *AIAA Paper* , 1569 (2009).
- [12] R. L. Jaffe, D. W. Schwenke, and G. Chaban, Vibrational and rotational excitation and dissociation in N_2 - N_2 collisions from accurate theoretical calculations, *AIAA Paper* , 1208 (2008).
- [13] E. V. Kustova, E. A. Nagnibeda, T. Y. Alexandrova, and A. Chikhaoui, Non-equilibrium dissociation rates in expanding flows, *Chemical Physics Letters* **377**, 663 (2003).
- [14] I. Armenise and E. V. Kustova, State-to-state models for CO_2 molecules: From the theory to an application to hypersonic boundary layers, *Chemical Physics* **415**, 269 (2013).
- [15] M. Panesi and A. Lani, Collisional radiative coarse-grain model for ionization in air, *Physics of Fluids (1994-present)* **25**, 057101 (2013).
- [16] T. E. Magin, M. Panesi, A. Bourdon, R. L. Jaffe, and D. W. Schwenke, Coarse-grain model for internal energy excitation and dissociation of molecular nitrogen, *Chemical Physics* **398**, 90 (2012).

- [17] A. Munafò, Y. Liu, and M. Panesi, Modeling of dissociation and energy transfer in shock-heated nitrogen flows, *Physics of Fluids* **27**, 127101 (2015).
- [18] Y. Liu, M. Panesi, A. Sahai, and M. Vinokur, General multi-group macroscopic modeling for thermo-chemical non-equilibrium gas mixtures, *The Journal of Chemical Physics* **142**, 134109 (2015).
- [19] A. Sahai, B. Lopez, C. O. Johnston, and M. Panesi, Adaptive coarse graining method for energy transfer and dissociation kinetics of polyatomic species, *The Journal of Chemical Physics* **147**, 054107 (2017).
- [20] M. Panesi, R. L. Jaffe, D. W. Schwenke, and T. E. Magin, Rovibrational internal energy transfer and dissociation of $N_2(^1\Sigma_g^+) - N(^4S_u)$ system in hypersonic flows, *The Journal of chemical physics* **138**, 044312 (2013).
- [21] C. O. Johnston and M. Panesi, Impact of state-specific flowfield modeling on atomic nitrogen radiation, *Physical Review Fluids* **3**, 013402 (2018).
- [22] C. O. Johnston, B. R. Hollis, and K. Sutton, Radiative heating methodology for the Huygens probe, *Journal of Spacecraft and Rockets* **44**, 993 (2007).
- [23] L. Soucasse, J. B. Scoggins, P. Rivière, T. E. Magin, and A. Soufiani, Flow-radiation coupling for atmospheric entries using a hybrid statistical narrow band model, *Journal of Quantitative Spectroscopy and Radiative Transfer* **180**, 55 (2016).
- [24] J. García-Garrido, A. S. Pudsey, and C. Mundt, Numerical simulations of radiative heat effects in a plasma wind-tunnel flow under Mars entry conditions, *Acta Astronautica* **151**, 334 (2018).
- [25] D. Yatsukhno, S. Surzhikov, D. Andrienko, J. Annaloro, and P. Omalý, Different estimations of the convective and radiative heating for the martian entry probes, *AIAA paper* , 0793 (2019).
- [26] L. Hartung, Predicting radiative heat transfer in thermo-chemical non-equilibrium flowfields, *NASA TM* **4564** (1994).

- [27] A. Munafò, A. Lani, A. Bultel, and M. Panesi, Modeling of non-equilibrium phenomena in expanding flows by means of a collisional-radiative model, *Physics of Plasmas* **20**, 073501 (2013).
- [28] A. M. Brandis and B. A. Cruden, NEQAIRv14.0 release notes: Nonequilibrium and equilibrium radiative transport spectra program, NASA TM (2014).
- [29] F. Liu, H. A. Becker, and A. Pollard, Spatial differencing schemes of the discrete-ordinates method, *Numerical Heat Transfer* **30**, 23 (1996).
- [30] P. J. Coelho, Advances in the discrete ordinates and finite volume methods for the solution of radiative heat transfer problems in participating media, *Journal of Quantitative Spectroscopy and Radiative transfer* **145**, 121 (2014).
- [31] R. Koch and R. Becker, Evaluation of quadrature schemes for the discrete ordinates method, *Journal of Quantitative Spectroscopy and Radiative Transfer* **84**, 423 (2004).
- [32] A. Sahai, N. N. Mansour, B. Lopez, and M. Panesi, Modeling of high pressure arc-discharge with a fully-implicit Navier–Stokes stabilized finite element flow solver, *Plasma Sources Science and Technology* **26**, 055012 (2017).
- [33] C. Park, *Nonequilibrium hypersonic aerothermodynamics* (Wiley, New York, 1990).
- [34] C. Johnston and M. Panesi, Advancements in afterbody radiative heating simulations for earth entry, AIAA Paper (2016).
- [35] S. Doraiswamy, J. D. Kelley, and G. V. Candler, Vibrational modeling of CO₂ in high-enthalpy nozzle flows, *Journal of Thermophysics and Heat Transfer* **24**, 9 (2010).
- [36] C. O. Johnston, B. R. Hollis, and K. Sutton, Spectrum modeling for air shock-layer radiation at lunar-return conditions, *Journal of Spacecraft and Rockets* **45**, 865 (2008).
- [37] I. Nompelis, T. W. Drayna, and G. V. Candler, Development of a hybrid unstructured implicit solver for the simulation of reacting flows over complex geometries, AIAA Paper **2227**, 2004 (2004).

- [38] I. Nompelis, T. W. Drayna, and G. V. Candler, A parallel unstructured implicit solver for hypersonic reacting flow simulation, in *Parallel Computational Fluid Dynamics 2005* (Elsevier, 2006) pp. 389–395.
- [39] G. V. Candler, H. B. Johnson, I. Nompelis, V. M. Gidzak, P. K. Subbareddy, and M. Barnhardt, Development of the us3d code for advanced compressible and reacting flow simulations, AIAA Paper , 1893 (2015).
- [40] E. V. Kustova and E. A. Nagnibeda, On a correct description of a multi-temperature dissociating CO₂ flow, *Chemical physics* **321**, 293 (2006).
- [41] E. V. Kustova and E. A. Nagnibeda, Kinetic model for multi-temperature flows of reacting carbon dioxide mixture, *Chemical Physics* **398**, 111 (2012).
- [42] J. S. Ogden, Introduction to molecular symmetry, *Oxford Chemistry Primers* **97** (2001).
- [43] K. Huber, G. Herzberg, and J. Gallagher, NIST chemistry webbook, NIST Standard Reference Database **69** (2011).
- [44] I. Armenise and E. Kustova, Mechanisms of coupled vibrational relaxation and dissociation in carbon dioxide, *The Journal of Physical Chemistry A* **122**, 5107 (2018).
- [45] E. V. Kustova and E. A. Nagnibeda, State-to-state theory of vibrational kinetics and dissociation in three-atomic gases, in *AIP Conference Proceedings* (IOP Institute of Physics Publishing Ltd, 2001) pp. 620–627.
- [46] Y. D. Shevelev, N. G. Syzranova, E. V. Kustova, and E. A. Nagnibeda, Numerical simulation of hypersonic flows around space vehicles descending in the Martian atmosphere, *Mathematical Models and Computer Simulations* **3**, 205 (2011).
- [47] P. V. Marrone and C. E. Treanor, Chemical relaxation with preferential dissociation from excited vibrational levels, *Physics of Fluids* (1958-1988) **6**, 1215 (1963).
- [48] Y. Liu, M. Vinokur, M. Panesi, and T. Magin, A multi-group maximum entropy model for thermo-chemical nonequilibrium, AIAA Paper (2010).

- [49] Y. Liu, M. Panesi, M. Vinokur, and P. Clarke, Microscopic simulation and macroscopic modeling of thermal and chemical non-equilibrium gases, AIAA paper **3146**, 2013 (2013).
- [50] R. Jaffe, Vibrational and rotational excitation and dissociation of CO₂ reexamined, AIAA Paper , 447 (2011).
- [51] E. Kustova, M. Mekhonoshina, and A. Kosareva, Relaxation processes in carbon dioxide, Physics of Fluids **31**, 046104 (2019).
- [52] S. A. Tashkun and V. I. Perevalov, CDS-4000: High-resolution, high-temperature carbon dioxide spectroscopic databank, Journal of Quantitative Spectroscopy and Radiative Transfer **112**, 1403 (2011).
- [53] C. O. Johnston, A. Sahai, and M. Panesi, Extension of multiband opacity-binning to molecular, non-Boltzmann shock layer radiation, Journal of Thermophysics and Heat Transfer , 1 (2017).
- [54] N. M. Laurendeau, *Statistical thermodynamics: Fundamentals and applications* (Cambridge University Press, 2005).
- [55] A. Wray, D. Prabhu, and J.-F. Ripoll, Opacity distribution functions applied to the CEV reentry, AIAA Paper , 4542 (2007).
- [56] V. I. Lebedev, Quadratures on a sphere, USSR Computational Mathematics and Mathematical Physics **16**, 10 (1976).
- [57] A. Mazaheri, C. O. Johnston, and S. Sefidbakht, Three-dimensional radiation ray-tracing for shock-layer radiative heating simulations, Journal of Spacecraft and Rockets **50**, 485 (2013).
- [58] I. Sohn, Z. Li, D. A. Levin, and M. F. Modest, Coupled DSMC-PMC radiation simulations of a hypersonic reentry, Journal of Thermophysics and Heat Transfer **26**, 22 (2012).

- [59] J. N. Reddy and D. K. Gartling, *The finite element method in heat transfer and fluid dynamics* (CRC press, 2010).
- [60] J. C. Chai, H. S. Lee, and S. V. Patankar, Finite volume method for radiation heat transfer, *Journal of thermophysics and heat transfer* **8**, 419 (1994).
- [61] A. Wray, Improved finite-volume method for radiative hydrodynamics, 7th International Conference on Computational Fluid Dynamics **505**, 1 (2012).
- [62] P. J. Coelho, A comparison of spatial discretization schemes for differential solution methods of the radiative transfer equation, *Journal of Quantitative Spectroscopy and Radiative Transfer* **109**, 189 (2008).
- [63] D. Joseph, M. El Hafi, R. Fournier, and B. Cuenot, Comparison of three spatial differencing schemes in discrete ordinates method using three-dimensional unstructured meshes, *International journal of thermal sciences* **44**, 851 (2005).
- [64] M. P. Adams, M. L. Adams, W. D. Hawkins, T. Smith, L. Rauchwerger, N. M. Amato, T. S. Bailey, and R. D. Falgout, *Provably optimal parallel transport sweeps on regular grids*, Tech. Rep. (Lawrence Livermore National Lab.(LLNL), Livermore, CA (United States), 2013).
- [65] F. C. Miranda, F. di Mare, A. Sadiki, and J. Janicka, Performance analysis of different solvers for computing the radiative transfer equation in complex geometries using finite volume method and block structured grids, *Computational Thermal Sciences: An International Journal* **9** (2017).
- [66] P. A. Gnoffo, R. N. Gupta, and J. L. Shinn, *Conservation equations and physical models for hypersonic air flows in thermal and chemical non-equilibrium.*, Technical Paper 2867 (NASA, 1989).
- [67] W. Huo, M. Panesi, and T. Magin, Ionization phenomena behind shock waves, in *High Temperature Phenomena in Shock Waves* (Springer, 2012) pp. 149–192.

- [68] A. Sahai, B. Lopez, C. O. Johnston, and M. Panesi, Novel approach for CO₂ state-to-state modeling and application to multidimensional entry flows, AIAA Paper , 0213 (2017).
- [69] B. J. McBride, M. J. Zehe, and S. Gordon, *NASA Glenn coefficients for calculating thermodynamic properties of individual species*, Technical Paper (NASA, 2002).
- [70] F. G. Blottner, M. Johnson, and M. Ellis, *Chemically reacting viscous flow program for multi-component gas mixtures.*, Tech. Rep. (Sandia National Laboratories, 1971).
- [71] R. N. Gupta, J. M. Yos, R. A. Thompson, and K. P. Lee, *A review of reaction rates and thermodynamic and transport properties for an 11-species air model for chemical and thermal non-equilibrium calculations to 30,000 K.*, Reference Publication 1232 (NASA, 1990).
- [72] C. Wilke, A viscosity equation for gas mixtures, The journal of chemical physics **18**, 517 (1950).
- [73] A. Sahai, *Modeling of high enthalpy flows for hypersonic re-entry and ground-based arc-jet testing*, Master's thesis, University of Illinois at Urbana-Champaign (2015).
- [74] G. V. Candler, Rate effects in hypersonic flows, Annual Review of Fluid Mechanics **51**, 379 (2019).
- [75] E. V. Kustova and G. M. Kremer, Effect of molecular diameters on state-to-state transport properties: The shear viscosity coefficient, Chemical Physics Letters **636**, 84 (2015).
- [76] E. Kustova, M. Mekhonoshina, and G. Oblapenko, On the applicability of simplified state-to-state models of transport coefficients, Chemical Physics Letters **686**, 161 (2017).
- [77] R. L. Macdonald, *Reduced-order model framework for thermochemical non-equilibrium hypersonic flows*, PhD dissertation, University of Illinois at Urbana-Champaign (2019).

- [78] J. M. Brock, P. K. Subbareddy, and G. V. Candler, Detached-eddy simulations of hypersonic capsule wake flow, *AIAA Journal* **53**, 70 (2014).
- [79] G. V. Candler, P. K. Subbareddy, and J. M. Brock, Advances in computational fluid dynamics methods for hypersonic flows, *AIAA Journal* **52**, 17 (2014).
- [80] G. V. Candler, C. R. Alba, and R. B. Greendyke, Characterization of carbon ablation models including effects of gas-phase chemical kinetics, *AIAA Journal* **31**, 512 (2017).
- [81] J. M. Brock, E. C. Stern, and M. C. Wilder, Computational fluid dynamics simulations of supersonic inflatable aerodynamic decelerator ballistic range tests, *Journal of Spacecraft and Rockets* , 1 (2018).
- [82] A. Brandis, C. Johnston, M. Panesi, B. Cruden, D. Prabhu, and D. Bose, Investigation of nonequilibrium radiation for mars entry, *AIAA Paper* , 1055.
- [83] A. Sahai, B. Lopez, C. O. Johnston, and M. Panesi, Novel approach for modeling co2 non-equilibrium radiation: Application to wake flows, *AIAA Paper* , 1051 (2019).
- [84] M. F. Modest, *Radiative heat transfer* (Academic Press, 2013).
- [85] M. J. Wright, C. Y. Tang, K. T. Edquist, B. R. Hollis, P. Krasa, and C. A. Campbell, A review of aerothermal modeling for Mars entry missions, *AIAA Paper* **443**, 4 (2010).
- [86] K. T. Edquist, B. R. Hollis, C. O. Johnston, D. Bose, T. R. White, and M. Mahzari, Mars science laboratory heat shield aerothermodynamics: Design and reconstruction, *Journal of Spacecraft and Rockets* **51**, 1106 (2014).
- [87] L. T. Xu, R. L. Jaffe, D. W. Schwenke, and M. Panesi, The effect of the spin-forbidden $\text{CO}(^1\Sigma^+) + \text{O}(^3\text{p}) \rightarrow \text{CO}_2(^1\Sigma_g^+)$ recombination reaction on afterbody heating of mars entry vehicles, *AIAA Paper* , 3486 (2017).
- [88] A. Kosareva and G. Shoen, Numerical simulation of a co2, co, o2, o, c mixture: Validation through comparisons with results obtained in a ground-based facility and thermochemical effects, *Acta Astronautica* (2019).

- [89] E. E. Whiting, C. Park, Y. Liu, J. O. Arnold, and J. A. Paterson, *NEQAIR96, Nonequilibrium and equilibrium radiative transport and spectra program: user's manual*, Tech. Rep. (NASA, 1996).
- [90] A. Alberti, A. Munafò, C. Pantano, J. Freund, and M. Panesi, Modeling of air breakdown by single-mode and multi-mode lasers, AIAA Paper , 1250 (2019).
- [91] C. O. Johnston, B. R. Hollis, and K. Sutton, Non-boltzmann modeling for air shock-layer radiation at lunar-return conditions, *Journal of Spacecraft and Rockets* **45**, 879 (2008).
- [92] S. Gu, *Mars entry afterbody radiative heating: An experimental study of nonequilibrium CO₂ expanding flow*, PhD dissertation, The University of Queensland (2018).
- [93] A. Gülhan, T. Thiele, F. Siebe, R. Kronen, and T. Schleutker, Aerothermal measurements from the ExoMars Schiaparelli capsule entry, *Journal of Spacecraft and Rockets* **56**, 68 (2018).